



Characteristics of anti-CD19 CAR T cell infusion products associated with efficacy and toxicity in patients with large B cell lymphomas

Qing Deng^{1,5}, Guangchun Han^{1,2,5}, Nahum Puebla-Osorio¹, Man Chun John Ma¹, Paolo Strati¹, Beth Chasen³, Enyu Dai², Minghao Dang², Neeraj Jain¹, Haopeng Yang¹, Yuanxin Wang², Shaojun Zhang^{1,2}, Ruiping Wang², Runzhe Chen², Jordan Showell¹, Sreejoyee Ghosh¹, Sridevi Patchva¹, Qi Zhang¹, Ryan Sun⁴, Frederick Hagemeister¹, Luis Fayad¹, Felipe Samaniego¹, Hans C. Lee¹, Loretta J. Nastoupil¹, Nathan Fowler¹, R. Eric Davis¹, Jason Westin¹, Sattva S. Neelapu¹, Linghua Wang^{1,2} and Michael R. Green^{1,2}

Autologous chimeric antigen receptor (CAR) T cell therapies targeting CD19 have high efficacy in large B cell lymphomas (LBCLs), but long-term remissions are observed in less than half of patients, and treatment-associated adverse events, such as immune effector cell-associated neurotoxicity syndrome (ICANS), are a clinical challenge. We performed single-cell RNA sequencing with capture-based cell identification on autologous axicabtagene ciloleucel (axi-cel) anti-CD19 CAR T cell infusion products to identify transcriptomic features associated with efficacy and toxicity in 24 patients with LBCL. Patients who achieved a complete response by positron emission tomography/computed tomography at their 3-month follow-up had three-fold higher frequencies of CD8 T cells expressing memory signatures than patients with partial response or progressive disease. Molecular response measured by cell-free DNA sequencing at day 7 after infusion was significantly associated with clinical response ($P = 0.008$), and a signature of CD8 T cell exhaustion was associated ($q = 2.8 \times 10^{-149}$) with a poor molecular response. Furthermore, a rare cell population with monocyte-like transcriptional features was associated ($P = 0.0002$) with high-grade ICANS. Our results suggest that heterogeneity in the cellular and molecular features of CAR T cell infusion products contributes to variation in efficacy and toxicity after axi-cel therapy in LBCL, and that day 7 molecular response might serve as an early predictor of CAR T cell efficacy.

Patients with LBCL who remain in complete response (CR) or partial response (PR) by imaging at 3 months after autologous anti-CD19 CAR T cell therapy have a significantly better outcome than those with stable disease (SD) or progressive disease (PD) before this point^{1,2}. This is likely owing to a combination of factors, such as the in vivo expansion and activity of CAR T cells after infusion and the development of tumor-intrinsic mechanisms of escape or resistance^{3–6}. Cellular features associated with response have been explored in the context of B cell leukemia and identified phenotypes within the apheresis product^{7,8} and CAR T cell infusion product^{9,10} as being important determinants. However, this has not been thoroughly investigated in the context of LBCL¹¹ and has yet to be systematically examined using single-cell transcriptomics.

Cytokine release syndrome (CRS) and ICANS are common adverse events associated with CAR T cell therapy^{12,13}. In adults with lymphoma treated with axi-cel, CRS is mostly low grade, but ICANS is more commonly high grade, with grade 3 or 4 (ICANSgr3–4) occurring in 30–45% of patients^{12,13}. Although reversible in most cases, ICANS prolongs hospitalization, requires intensive care in a subset of patients, delays recovery and increases the cost of care. Less commonly, seizures and cerebral edema have

been noted with ICANS and have been fatal in some patients. Although the pathophysiology of CRS has been studied extensively, and appropriate management strategies with anti-interleukin (IL)-6 therapy have been developed^{12,14–16}, the pathophysiology of ICANS and its optimal management are less clear. The development of ICANS is associated with a high level of inflammatory cytokines within circulation and in the cerebrospinal fluid^{17–19}, with monocyte-derived IL-1 being recently highlighted as a key driver of neurotoxicity²⁰. Increased permeability of the blood-brain barrier might allow these cytokines and immune cells to enter the central nervous system and contribute to neurological inflammation^{18,19}. However, the features of CAR T cells that drive this hyper-inflammatory state in some patients and not others are currently unknown.

We hypothesized that the heterogeneity of autologous CAR T cell infusion products might contribute to the inter-patient variability in efficacy and toxicity and investigated this by performing single-cell RNA sequencing (scRNA-seq) of standard-of-care axi-cel infusion products administered to patients with LBCL. We thereby identified features associated with clinical response, molecular response and the development of ICANSgr3–4. These data provide new insights

¹Department of Lymphoma and Myeloma, The University of Texas MD Anderson Cancer Center, Houston, TX, USA. ²Department of Genomic Medicine, The University of Texas MD Anderson Cancer Center, Houston, TX, USA. ³Department of Nuclear Medicine, The University of Texas MD Anderson Cancer Center, Houston, TX, USA. ⁴Department of Biostatistics, The University of Texas MD Anderson Cancer Center, Houston, TX, USA. ⁵These authors contributed equally: Qing Deng, Guangchun Han. e-mail: sneelapu@mdanderson.org; lwang22@mdanderson.org; mgreen5@mdanderson.org

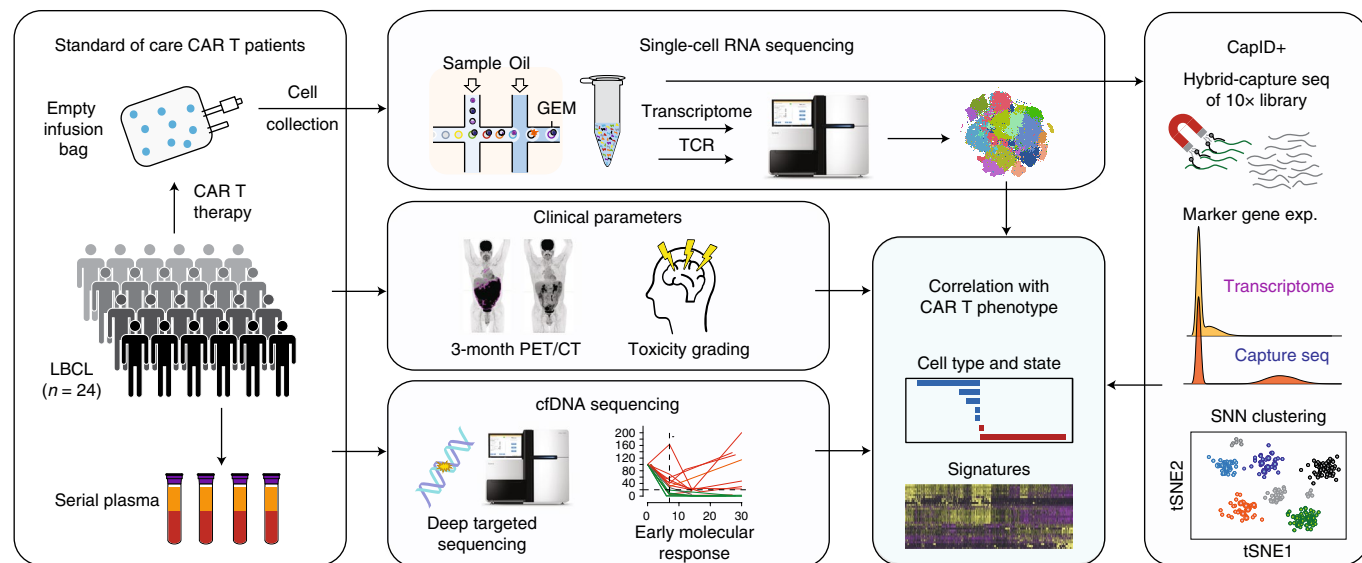


Fig. 1 | Study design. A schematic overview of the experimental design and bioinformatics flow for scRNA-seq analysis of 137,276 residual cells from CAR T cell infusion products of 24 patients with LBCL. Our approach incorporated single-cell transcriptome profiling of CAR T cell infusion products boosted by CapID+, correlation of single-cell functional states and gene expression signatures with efficacy assessed by PET/CT and cfDNA sequencing and with toxicity assessed by clinical grading.

into the cellular and molecular basis for inter-patient variability in CAR T cell efficacy and toxicity.

Results

Gene expression signatures of CAR T cell infusion products determined by scRNA-seq and CapID+. An overview of our approach is shown in Fig. 1. We performed whole-transcriptome scRNA-seq of 137,326 residual cells obtained from washing the standard-of-care axi-cel product bags after infusion of the CAR T cells into 24 patients with LBCL (16 diffuse large B cell lymphoma (DLBCL), six transformed follicular lymphoma (tFL) and two primary mediastinal B cell lymphoma (PMBCL); Supplementary Table 1). Each sample was run fresh for library preparation; thus, each sample was its own batch, and ‘batch effect’ could not be formally assessed. However, clusters were defined by genes associated with cell states (Extended Data Fig. 1); cells from all samples were interspersed across multiple clusters; and all clusters contained cells from multiple samples (Fig. 2a,b and Supplementary Fig. 1).

Cell types and functional states were defined according to previously described marker genes²¹. To improve this classification, we employed hybrid-capture sequencing of marker genes and the CAR construct sequence from scRNA-seq libraries and refined CD4 and CD8 classification by shared nearest neighbor (SNN) clustering (CapID+; Supplementary Table 2 and Methods). This approach does not rescue transcript dropout that results from failure of a messenger RNA molecule to be reverse transcribed in the gel beads in emulsion (GEMs). Rather, CapID increases the sequencing saturation of informative genes (Extended Data Fig. 2), thereby increasing the sensitivity of detection and signal-to-noise ratio for these transcripts within a given library (Fig. 2c). This rescued cell identities (Fig. 2d) and led to a more significant correlation with flow cytometry-based measurement of cell frequencies (Extended Data Fig. 3). Our CapID+ methodology, therefore, allows for the accurate assignment of CAR status and cellular gene expression. CAR expression was interspersed across the clusters (Fig. 2d) and was associated with few significant differences in gene expression compared to non-transformed T cells (Extended Data Fig. 4).

We, therefore, did not separate CAR-positive and CAR-negative cells for subsequent analyses.

Cell signatures associated with clinical response. At the 3-month follow-up by positron emission tomography/computed tomography (PET/CT)—a clinically relevant surrogate time point to predict long-term durability of response after axi-cel therapy in LBCL¹—13 patients had PD (50%), one was in PR (4%), nine were in CR (38%) and one was not evaluable (NE). We compared the representation of cell types and functional states between the infusion products from patients in CR and those in PR/PD. This revealed a significant enrichment of exhausted CD8 and CD4 T cells within the infusion products of patients with PR/PD and a significant enrichment of memory CD8 T cells within the infusion products of patients who achieved CR (Fig. 3a).

We then identified differentially expressed genes (DEGs) between CD8 T cells from patients with CR compared to patients with PR/PD (Supplementary Table 3) followed by unsupervised hierarchical clustering using the DEGs (Fig. 3b). Four cell clusters were identified with cells that showed differential expression of the genes associated with CR or PR/PD, respectively. Each cluster contains cells from all patients, but the relative proportions of cells from patients with CR significantly differ across the clusters ($P < 2.2 \times 10^{-16}$). Cells within the C1 cluster expressed the highest levels of genes associated with PR/PD, had the lowest level of genes associated with CR, had the lowest proportion of cells from patients with CR (19%) and are characterized by high expression of genes encoding lymphocyte activation 3 (LAG3)²², the exhaustion-associated transcription factors basic leucine zipper ATF-like transcription factor (BATF)^{23,24} and inhibitor of DNA binding 2 (ID2)^{25,26}, interferon gamma (IFNG), effector molecules (GZMA, GZMB and GNLY) and major histocompatibility class II (MHCII) molecules. These genes are associated with activation and exhaustion of CD8 T cells, in line with our observed enrichment of exhausted CD8 T cells in patients with PR/PD (Fig. 3a). We, therefore, evaluated the expression of a previously defined CD8 T cell dysfunction signature²⁷ by single-cell gene set variation analysis (scGSVA). This signature was highest in the C1 cluster, with

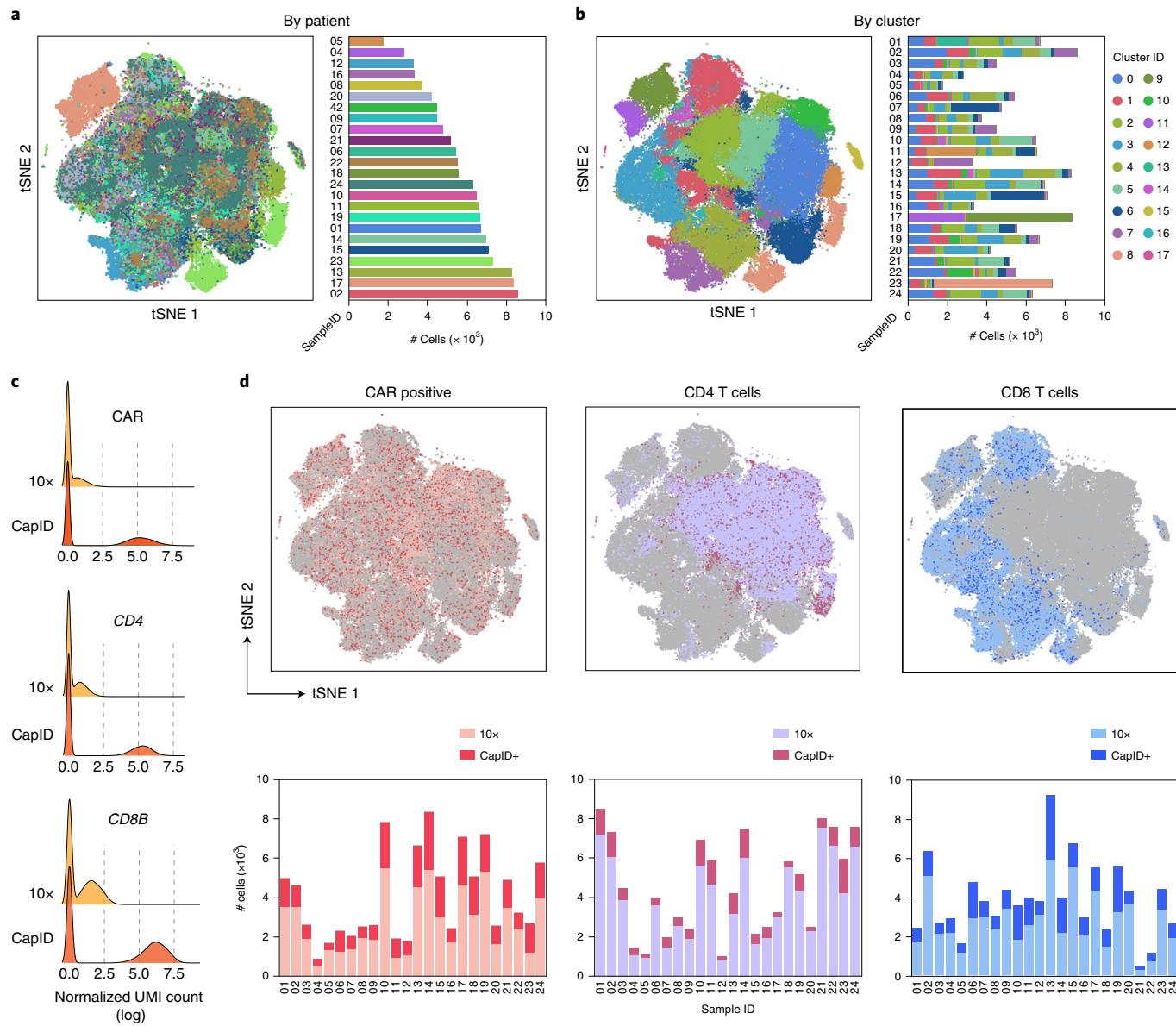


Fig. 2 | Single-cell analysis of standard-of-care CAR T cell infusion products. **a**, An overview of the 133,405 cells that passed QC for subsequent analyses in this study. Cells are color coded by the corresponding patient origin (sample ID) in the tSNE plot and a bar graph showing the number of cells per patient that passed QC. **b**, Cells are color coded by tSNE cluster number and a bar graph showing the distribution of cells from each patient among clusters. **c**, Individually scaled density plots show the normalized expression for the CAR, CD4 and CD8B transcripts in 10x scRNA-seq data and CapID hybrid capture sequencing data derived from the same scRNA-seq libraries. Histogram overlays with identical scaling showing the relative fraction of cells with zero counts are shown in Extended Data Fig. 2b. **d**, The tSNE overview and bar graph summary of the cells identified as being CAR positive (left), CD4 T cells (middle) and CD8 T cells (right) using 10x scRNA-seq data and those rescued by CapID+.

progressively less expression in the C2 and C3 clusters and the lowest expression in the C4 cluster (Fig. 3b,c). The features associated with activation and exhaustion in cells predominantly originating from patients with PR/PD are, therefore, linked with a profile of CD8 T cell dysfunction. Cells within the C2 and C3 clusters have variable expression of genes that were associated with CR or PR/PD, respectively, and a mixed representation of cells from patients with CR and PR/PD. Cells within the C4 cluster had the lowest expression of genes associated with PR/PD, the highest expression of genes associated with CR and the highest proportion of cells originating from patients who achieved CR (65%). These cells were characterized by high expression of genes associated with a central memory phenotype, such as *CCR7*, *CD27* and *SELL* (Fig. 3b and Supplementary

Fig. 2a), but not markers associated with a CD8 stem cell memory phenotype (Supplementary Fig. 2b). This, too, was in line with the enrichment of CD8 memory T cells in products from patients with CR when comparing the frequencies of functional states (Fig. 3a). Specifically, CD8 T cells from the infusion products of patients who achieved CR had a ~threefold higher fraction of *CCR7*⁺*CD27*⁺ double-positive CD8 T cells compared to cells from patients with PR/PD (Fig. 3d). The frequency of these cells were also low in patients with high-stage disease (III and IV) and high international prognostic index (IPI 3–4), suggesting that clinical factors might influence the transcriptional state of CAR T cells (Supplementary Fig. 3a). As *CCR7* and *CD27* can be expressed on naive T cells, we used scGSEA to measure the expression of a previously defined

CD8 memory signature²¹. Cells within the C4 cluster had the highest expression of the CD8 memory signature, with progressively lower levels of expression in the C3 and C2 clusters and the lowest expression in the C1 cluster (Fig. 3c). Our observations from comparing functional states and DEGs were further corroborated by scGSVA analysis of the association between unselected gene sets and patient outcome, which confirmed the high expression of activation and exhaustion signatures, such as PD-1 and IFN- γ signaling in CD8 T cells from patients with PR/PD, and the high expression of immune memory signatures²⁸ in CD8 T cells from patients who achieved CR (Fig. 3e, Supplementary Fig. 4 and Supplementary Table 4).

DEG analysis and unsupervised clustering of CD4 T cells revealed some similarities with the profiles of CD8 T cells, such as higher expression of *CCL5*, *GNLY* and *MHCII* genes in clusters with high frequencies of cells from patients with PR/PD (C1 and C2) and low frequencies of cells from patients with CR (C3–5) (Fig. 3f). Cluster C2 consisted only of cells that originated from the infusion products of patients with PR/PD and was characterized by a high expression of *TIGIT*²⁹ (Supplementary Fig. 5). However, in CD4 T cells, there was higher expression of proliferation-associated genes and cycling cells within clusters with high frequencies of cells from patients who achieved CR (Fig. 3f and Supplementary Table 5). This was confirmed by scGSVA analysis, showing an enrichment of proliferation-associated gene sets in CD4 T cells from patients who achieved CR (Fig. 3e, Supplementary Fig. 4 and Supplementary Table 6).

These data highlight important transcriptional signatures of cells within CAR T cell infusion products that are associated with clinical efficacy. The mixture of cells from patients with CR and PR/PD across multiple clusters is consistent with each infusion product containing cells of both desirable (signatures associated with CR) and undesirable (signatures associated with PR/PD) states and the relative proportion of these states within each CAR T cell infusion product being linked with efficacy.

A CD8 T cell exhaustion signature associated with failure to achieve an early molecular response. Antigen-driven CAR T cell expansion reaches its peak approximately 1 week after axi-cel infusion⁴. We, therefore, hypothesized that assessment of response dynamics within the first week of treatment might provide insights into CAR T cell clinical activity. We investigated this by interrogating patterns of early molecular response (EMR) determined by plasma-derived cell-free DNA (cfDNA) sequencing with a previously described hybrid-capture panel³⁰ (Methods). Somatic mutations identified at infusion (days 0–1) were used to measure the

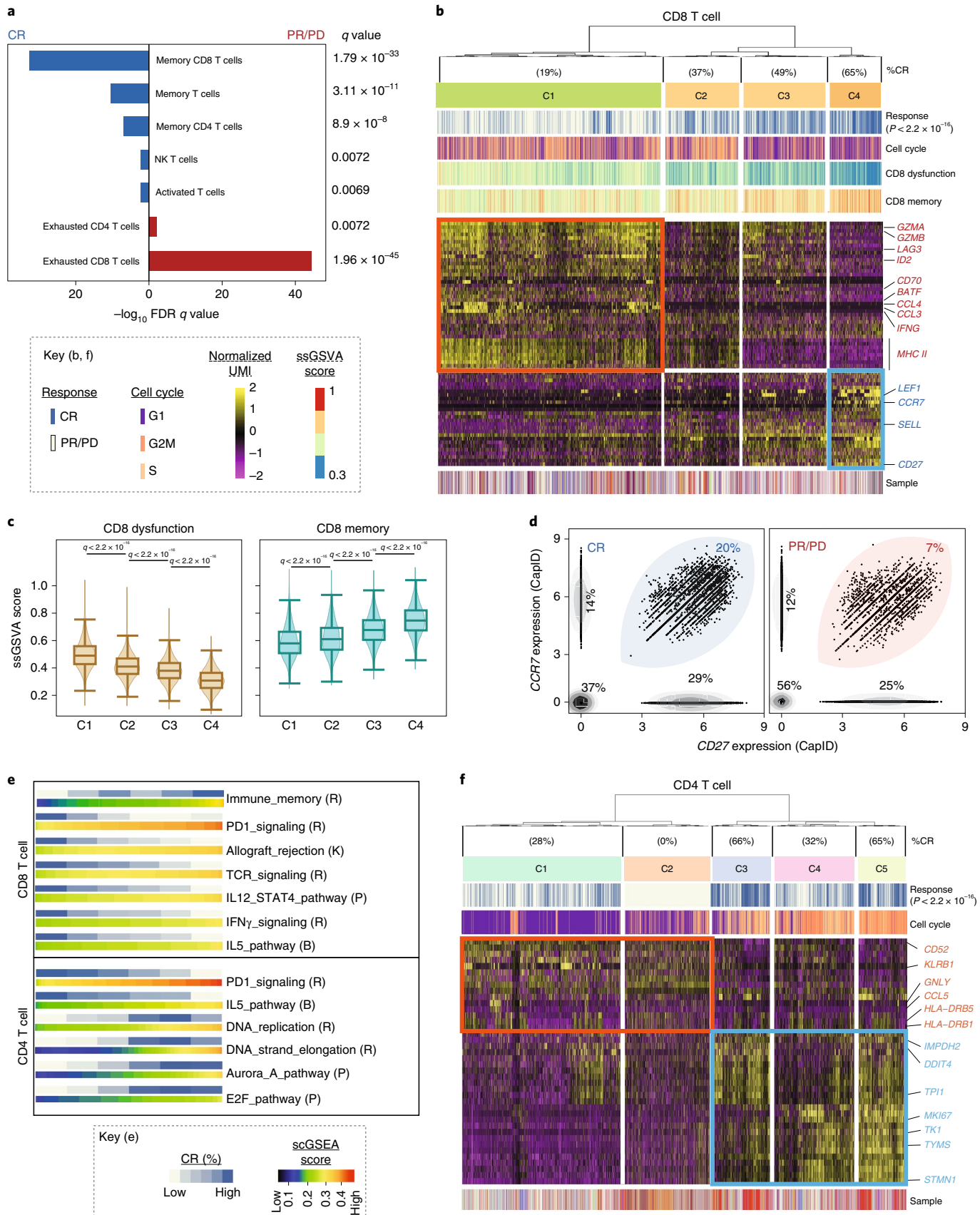
relative changes in variant allele fractions (VAFs) at 1 week ($n=22$), 2 weeks ($n=18$) and 1 month ($n=16$) after infusion. Of 22 patients with available samples, 17 had three or more somatic mutations detected at days 0–1 for disease monitoring (Supplementary Table 7). Neither the number of calibrated mutations nor the VAF at day 0 was associated with subsequent response (Extended Data Fig. 5). VAF declined within the first week of treatment for 16 of 17 patients, and the magnitude of decline was significantly associated with ongoing CR by PET/CT at 3 months (two-sided Wilcoxon rank-sum test, $P=0.008$; Fig. 4a,b). We applied a threshold of five-fold reduction in VAF to dichotomize patients evaluable for response. Of the eight patients with more than five-fold molecular response (>5FMR), six (75%) had ongoing CR at 3 months. Two patients (ac17 and ac21) with >5FMR at day 7 progressed by the time of their 3-month PET/CT, consistent with the ~16% of patients in the ZUMA-1 pivotal study of axi-cel who had a CR at their 1-month evaluation but progressed before their 3-month follow-up⁴. Notably, these patients had an observable increase in their VAFs at day 14 or day 30 (Extended Data Fig. 5). Of the eight evaluable patients with less than five-fold molecular response (<5FMR), none was in CR at their 3-month follow-up (0%). Patients with <5FMR also showed a trend toward reduced CAR T cell expansion, as measured by quantitative polymerase chain reaction (PCR) analysis of the CAR transcript from cfDNA (Supplementary Fig. 6). The association between EMR and long-term outcome after CAR T cell therapy requires prospective validation in a large independent cohort but supported its use as a relevant metric to evaluate using scRNA-seq.

Comparison of the cellular functional states within products from patients with >5FMR versus <5FMR revealed a striking association between transcriptional profiles of T cell exhaustion and a poor EMR (Fig. 5a). This was particularly significant within the CD8 T cell compartment. All of the co-inhibitory receptor genes used to classify exhausted CD8 T cells were expressed in a higher fraction of CD8 T cells from patients with <5FMR compared to >5FMR (Fig. 5b; $q<0.01$). Of these, *LAG3* and *TIM3* were the most abundantly expressed, and cells co-expressing both *LAG3* and *TIM3* were highly discriminatory between the <5FMR and >5FMR groups (Fig. 5b; $q<2.38 \times 10^{-170}$). Specifically, 36.8% of CD8 T cells from patients with <5FMR were *LAG3*⁺*TIM3*⁺ compared to 22.7% from patients with >5FMR (Fig. 5c). Frequencies of *LAG3*⁺*TIM3*⁺ cells were only moderately higher in infusion products of patients with PR/PD compared to patients with CR determined by their 3-month PET/CT (Supplementary Fig. 7) and not significantly different between memory CD8 T cells compared to other CD8 T cells (Supplementary Fig. 7). The frequency of *LAG3*⁺*TIM3*⁺ CD8 T cells was also higher in patients with high IPI (3–4) and lower in

Fig. 3 | Molecular phenotypes of CAR T cell infusion products associated with response determined by PET/CT. **a**, Cell types and functional states that were significantly more frequent in CAR T cell products from patients with continued CR at 3 months (blue) or those from patients with PR/PD (red). q values were calculated by a two-sided Fisher's exact test with a Benjamini-Hochberg correction. **b**, Heat map of four CD8⁺T cell clusters (C1–C4) generated from unsupervised clustering of genes that were differentially expressed in CD8 T cells from the infusion products of patients with CR compared to those from patients with PR/PD. A color-coded track shows the cells that originated from infusion products of CR patients (blue, CR) and the percentage of these cells within each cluster labeled at the top. Additional tracks show the scGSVA scores of CD8 dysfunction and CD8 memory signatures, respectively, and the inferred cell cycle status. The percentage of cells that originated from infusion products of CR patients is significantly different between clusters (one-way analysis of variance, $P<2.2 \times 10^{-16}$). The corresponding sample origins are labeled at the bottom, colored as per Fig. 2a. **c**, Violin plots show the scGSVA scores of cells from each of the four clusters in Fig. 2b. C1, $n=26,917$ cells; C2, $n=9,047$ cells; C3, $n=10,113$ cells; C4, $n=6,440$ cells. Box, median \pm interquartile range; whiskers, 1.5 \times interquartile range. Pairwise comparisons were performed using a two-sided Wilcoxon rank-sum test with a Benjamini-Hochberg correction. **d**, Scatter plots of *CCR7*⁺*CD27*⁺ CD8 T cells measured by CapID in the infusion products of patients who achieved CR compared to those who had PR/PD (two-sided Fisher's exact test, $P<2.2 \times 10^{-16}$). **e**, Gene sets that are significantly positively (+) or negatively (-) associated with CR in CD8 (above) or CD4 (below) T cells. For each pathway, a heat map of the scGSVA scores are shown, with percentage of cells originated from infusion products of CR patients annotated on the top. The origin of the gene set is shown in brackets (B, biocarta; R, reactome; K, KEGG; P, PID). **f**, A heat map of five CD4⁺ T cell clusters (C1–C5) determined by unsupervised clustering of genes that were differentially expressed in CD4 T cells from infusion products of patients with CR compared to those from patients with PR/PD. The percentage of cells that originated from infusion products of CR patients is shown in a track at the top and is significantly different between clusters (one-way analysis of variance, $P<2.2 \times 10^{-16}$). Cells are annotated by inferred cell cycle state and sample origin as in **b**.

patients who had received an autologous stem cell transplantation before their CAR T cell therapy (Supplementary Fig. 3). Patients with poor responses had moderately reduced T cell receptor (TCR)

clonotypic diversity (Extended Data Fig. 6), but higher rates of the CD8 T cell exhaustion signature were not due to the presence of highly expanded and exhausted clonotypes. Rather, each clonotype



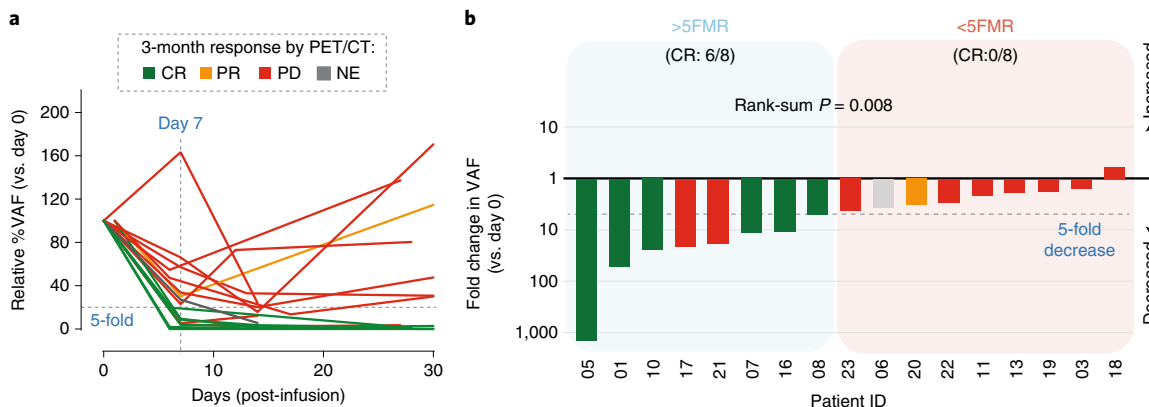


Fig. 4 | Association between EMR measured by cfDNA sequencing and clinical response measured by PET/CT. **a**, Molecular response measured by deep targeted cfDNA sequencing over the first month after infusion. VAFs for each patient ($n=17$) are normalized to the infusion day time point (day 0), and lines are colored according to response assessed by PET/CT at their 3-month follow-up or prior disease progression. **b**, Fold change in molecular disease burden at the day 7 time point relative to the day 0 time point is shown for each patient, with bars colored by clinical response determined by PET/CT at their 3-month follow-up. The fold reduction of molecular disease burden was significantly associated with clinical response at 3 months (two-sided Wilcoxon rank-sum test, $P=0.008$). The 16 patients with evaluable response were split into two groups according to whether they achieved $>5\text{FMR}$ or $<5\text{FMR}$.

from patients with $<5\text{FMR}$ had a significantly higher fraction of $LAG3^+TIM3^+$ cells compared to patients with $>5\text{FMR}$ (Fig. 5d; $P=4.8 \times 10^{-9}$), indicating that T cells with the exhaustion signature are polyclonal. Further studies to examine the cytotoxicity and proliferative capacity of $LAG3^+TIM3^+$ CD8 T cells are required to validate that this profile is associated with a loss of effector function and/or *in vivo* expansion of CD8 CAR T cells, respectively.

We next investigated whether the $LAG3^+TIM3^+$ CD8 T cell signature is important in the setting of CAR T cell failure. Using CapID+ analysis of fresh core needle biopsies of nine LBCL tumors, we compared the frequencies of tumor-infiltrating $LAG3^+TIM3^+$ CD8 T cells between five tumors from patients who had never received CAR T cell therapy (CAR T naive) and from four patients who progressed after axi-cel with PR/PD as best response (post-CAR T; Fig. 5e and Supplementary Table 8). There was no significant difference in the number of preceding lines of therapy between these cohorts. This showed that 34% (1,402/4,114) of CD8 T cells within tumors progressing from CAR T cell therapy were $LAG3^+TIM3^+$, as compared to 19% (587/3,168) from CAR T naive tumors progressing from chemo-immunotherapy. CAR⁺ T cells were detectable in all tumors from patients who progressed after axi-cel and are the only cells that can be definitively traced to the CAR T cell infusion product. Fifty-one percent (295/589) of CAR⁺ CD8 T cells within tumors progressing from axi-cel were $LAG3^+TIM3^+$ (Fig. 5e). Patients who do not achieve a robust EMR, therefore, have a significantly higher frequency of CD8 T cell exhaustion signatures characterized by increased proportion of $LAG3^+TIM3^+$ cells, which is a signature that is proportionately over-represented among intratumoral CD8 T cells from patients progressing from axi-cel CAR T cell therapy.

Cells with a monocyte-like transcriptional signature are associated with high-grade ICANS. We aimed to identify features of the CAR T cell infusion products that were significantly associated with related toxicities. We first evaluated differences between patients who developed high-grade CRS ($n=4$) and patients who did not ($n=20$). Although the number of patients with high-grade CRS was small, we observed a negative association with exhausted CD8 T cells and a positive association with exhausted CD4 T cells (Extended Data Fig. 7 and Supplementary Tables 9 and 10). However, CRS is effectively managed with the use of corticosteroids and IL-6/IL-6R antagonists¹³, which might have confounded these results.

We next evaluated differences between patients who developed ICANSgr3–4 ($n=12$) and patients with ICANSgr0–2 ($n=12$). We did not observe significant differences in gene expression within the major CD4 or CD8 T cell compartments, but patients with ICANSgr3–4 had a significantly lower frequency of CAR⁺ cells within their infusion products (Extended Data Fig. 8). As axi-cel dosing is calculated based on transduction efficiency to achieve 2×10^6 CAR-positive cells per kilogram, this association might suggest that higher total cell doses per kilogram contributes to neurological toxicity, but this requires validation. We further evaluated whether ICANSgr3–4 is associated with any unique cluster of cells with distinct transcriptomic features, which identified a small cluster ($n=254$) that was significantly over-represented in the infusion products of patients who developed ICANSgr3–4 (Fig. 6a). These cells were unlikely to be cellular debris or doublets (Supplementary Fig. 8) and are henceforth referred to as ICANS-associated cells (IACs). A significantly lower fraction of IACs had detectable CAR expression (10.6% IACs versus 36.2% other cells; two-tailed Wilcoxon rank-sum test, $P < 0.001$), TCR rearrangements (14.6% IACs versus 92% other cells; two-tailed Wilcoxon rank-sum test, $P < 0.001$), *CD3D* expression (22.4% IACs versus 93.3% other cells; two-tailed Wilcoxon rank-sum test, $P < 0.001$) and *CD8B* expression (4.3% IACs versus 49.3% other cells; two-tailed Wilcoxon rank-sum test, $P < 0.001$; Fig. 6b,c) compared to cells from other clusters. Expression of *CD4* was detected in 49.6% of IACs compared to 32.9% of other cells, but this can be expressed on both the myeloid and T lymphoid lineages in response to IL-2 (refs. ^{31,32}). We identified 257 genes with significantly higher expression in IACs compared to other cells (two-sided Wilcoxon rank-sum test, $q < 0.01$, fold change >2 ; Supplementary Table 11), including multiple genes that are typically expressed within the myeloid lineage, such as *CD68*, *LYZ*, *SPI1*, *LILRB4* and *SIRPA* (Fig. 6b–d). Multiple cytokines and chemokines were among the genes with significantly higher expression in IACs compared to other cells, including *IL1B* and *CXCL8* (*IL8*), which have been previously implicated in ICANS pathophysiology^{17,20}. These cytokines were higher in the serum of patients with IACs, but this was part of a broad pattern of inflammation¹⁷ (Extended Data Fig. 9). Using single-sample gene set enrichment analysis (ssGSEA) of the IAC signature genes within profiles from purified hematopoietic cell subsets³³, we observed that the IAC signature was significantly higher in cells of myeloid lineages than

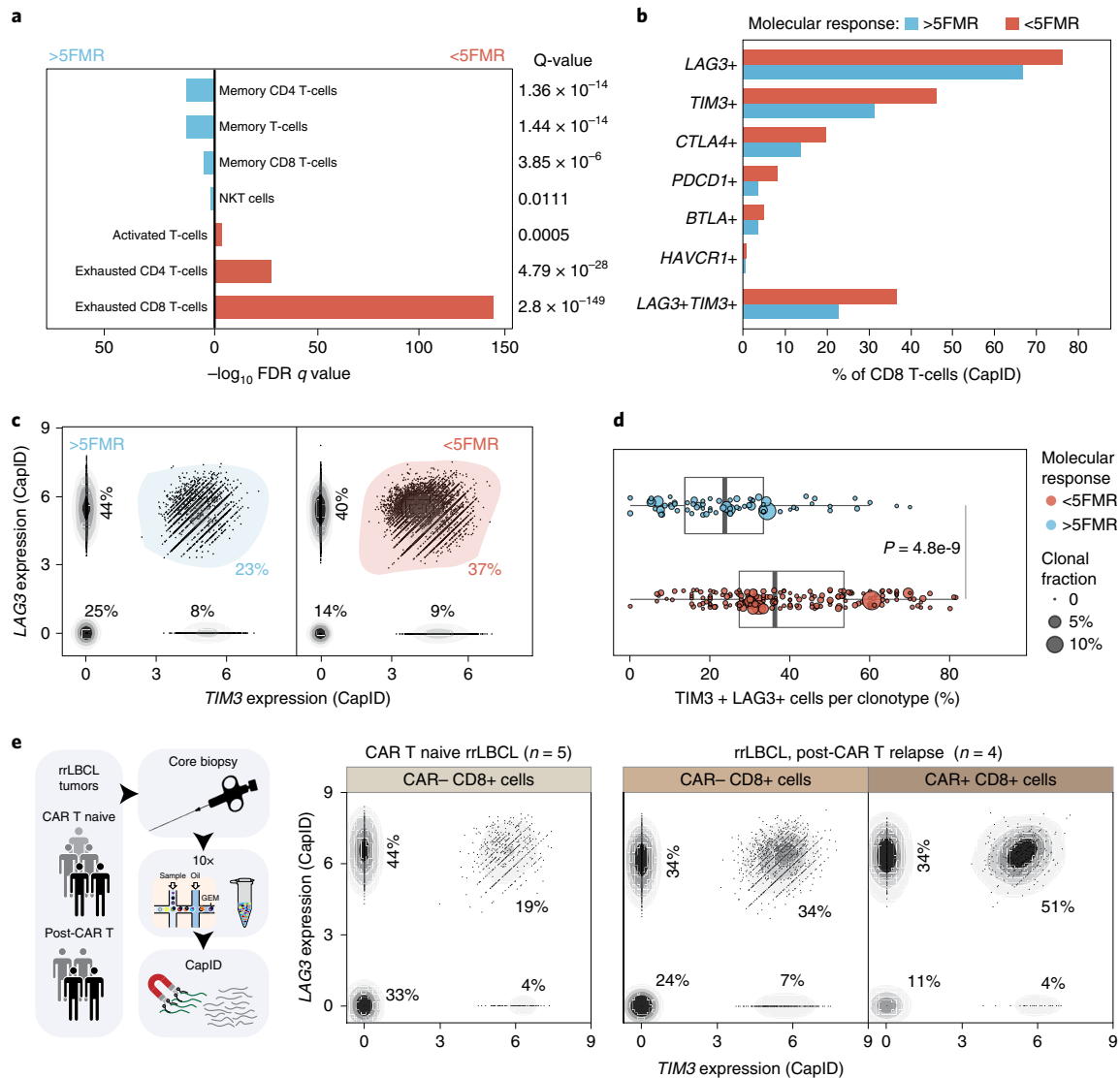


Fig. 5 | Association between CD8 T cell exhaustion markers and EMR. **a**, Cell types and functional states associated with more than five-fold molecular response at day 7 (>5FMR, blue) or failure to achieve five-fold molecular response at day 7 (<5FMR, red). *q* values were calculated by a two-sided Fisher's exact test with a Benjamini-Hochberg correction. **b**, The percentage of cells expressing co-inhibitory molecules used in the classification of exhausted CD8 T cells, and the percentage of cells co-expressing *LAG3* and *TIM3*, is shown for cells from patients with >5FMR (turquoise) compared to those from patients with <5FMR (red). **c**, Scatter plots show the expression of *LAG3* and *TIM3* in cells from patients who achieved >5FMR (left, blue) compared to those from patients with <5FMR (right, red). Each point represents a single cell, and the proportion of cells at each state is labeled on the plot. Expression levels are normalized UMI counts from CapID sequencing, with normalized UMI counts of more than 2 defined as positive expression. **d**, The percentage of cells from each TCR clonotype (identified from single-cell TCR sequencing) co-expressing *LAG3* and *TIM3* are shown, and data are compared between clonotypes within infusion products from patients with >5FMR (above, blue) and those from patients with <5FMR (below, red). The size of each point indicates the clonal fraction of each clonotype within each infusion product. >5FMR: *n* = 72 clonotypes from eight patients; <5FMR: *n* = 196 clonotypes from nine patients. Boxes, median ± the interquartile range; whiskers, 1.5x interquartile range. *P* values were calculated by two-sided Wilcoxon rank-sum tests. **e**, Transcripts were measured in 38,601 cells from fresh core needle biopsies of nine relapsed-refractory LBCL tumors by CapID; from five patients progressing after chemo-immunotherapy or targeted therapy (CAR T naive); and from four patients progressing after axi-cel CAR T cell therapy (post-CAR T). The expression of *TIM3* and *LAG3* was quantified by CapID within CD8 T cells in CAR T naive and post-CAR T tumors and within CD8 T cells expressing the CAR transcript in post-CAR T tumors. The fraction of single- and double-positive cells was annotated.

in cells of lymphoid lineages ($P < 2.2 \times 10^{-16}$) and highest in classical monocytes (Fig. 6e). However, IACs did not express genes encoding canonical monocyte markers, such as *CD14* or *CD16* (*FCGR3A* and *FCGR3B*) (Fig. 6c). Therefore, despite the similarities of the IACs' transcriptional signature to monocytes, the expression of *CD3D* on 22.4% of IACs and the lack of expression of canonical monocyte cell markers means that we cannot confidently assign these cells to the monocyte lineage.

We validated the IAC population within the original cohort plus an additional 16 patients (total, *n* = 40; Supplementary Table 1) using an approach that is statistically independent of clustering. Specifically, the IAC signature genes (Supplementary Table 2) were measured by CapID, and the signature was quantified by scGSVA (Extended Data Fig. 10). Of the 254 IACs identified by clustering of transcriptome data, 231 were classified as IACs with high confidence using CapID and scGSVA. An additional 184 IACs were identified

among 131,924 cells from the 16-patient validation cohort. IACs were both qualitatively and quantitatively associated with the development of ICANSgr3–4 (Fig. 6f). Eleven of 18 patients (61.1%) who developed ICANSgr3–4 had detectable IACs within their infusion products, compared to 2 of 22 patients (9.1%) with ICANSgr0–2 (two-sided Fisher's exact test, $P = 0.0007$). IACs consisted of a mean of 0.39% of cells (range, 0–2.27%) from patients with ICANSgr3–4, compared to 0.003% of cells from patients with ICANSgr0–2 (range, 0–0.4%; 130-fold higher in ICANSgr3–4; Wilcoxon rank-sum test, $P = 0.0002$). All patients with grade 4 ICANS (3/3) had detectable IACs, but the difference between patients with grade 3 versus grade 4 was not significant (Supplementary Fig. 9). It will be important to investigate the origin and function of IACs in future studies and to validate their potential predictive capacity for ICANSgr3–4 in a large prospective series.

Discussion

Our results suggest that cellular and molecular diversity of infused CAR T cell products is a major factor contributing to the variability in efficacy and toxicity among patients with LBCL treated with CD19 CAR T cell therapy. Quantifiable phenotypes associated with the infusion product are potentially actionable by enriching desirable, or depleting undesirable, cellular populations or functional states during manufacturing. Furthermore, our understanding of the mechanisms by which discrete cellular populations lead to poor response or high-grade toxicity might identify avenues for therapeutic intervention to improve efficacy and decrease toxicity after CAR T cell infusion.

We did not observe significant differences in gene expression profiles between cells expressing the CAR transcript compared to those with no detectable CAR expression, presumably because the signaling induced by stimulation during the manufacturing process might overwhelm the effects of any tonic signaling originating from the CAR construct. Comparisons of CAR transduced and untransduced T cells will, therefore, need to be performed separately using cells isolated from patients after infusion, when the transcriptional consequences of tonic or antigen-driven signaling will be more evident. We showed that cells from the infusion products of patients with ongoing CR at 3 months had an enrichment of CD8 memory T cell phenotypes compared to patients with PR/PD. This is in line with a previous study that evaluated CAR T cells with CD3ζ and 4-1BB signaling domains in the setting of chronic lymphocytic leukemia, in which a memory CD8 phenotype was associated with superior responses¹⁰. However, we observed a high expression of CCR7 that is consistent with a central memory phenotype. Manufacturing conditions or rapid expansion protocols can be adapted to favor the generation of central memory CD8 T cells^{34,35}, which we would expect to be associated with greater efficacy.

Patients with PR/PD had a significant enrichment of cells with a CD8 T cell exhaustion signature within their infusion products, and this association was most significant in patients who did not achieve a robust EMR at day 7. This is consistent with the kinetics of CAR T cell expansion, which peaks ~1 week after axi-cel infusion and declines thereafter. Tumor-derived somatic alterations can be readily detected in the cfDNA of patients with DLBCL^{30,36–38} and have been shown to correlate with tumor burden measured by functional imaging³⁶. The kinetics of tumor-derived cfDNA after chemo-immunotherapy might be predictive of patient outcome^{37,38}, but, to our knowledge, this has not been previously examined in patients treated with CD19 CAR T cells. Furthermore, no other metrics are available to predict the outcome of patients with LBCL treated with CD19 CAR T cells before their first clinical assessment at 1 month after infusion. In our cohort, the magnitude of EMR was correlated with efficacy assessed at the 3-month follow-up by PET/CT. This association requires prospective validation in a large independent series but raised the possibility that failure to achieve EMR within the first week might be a biomarker for poor CAR T cell function. In line with this notion, we observed a significant association between poor EMR and gene expression signatures associated with T cell exhaustion. Other studies aimed at addressing exhaustion of CAR T cells have primarily focused on targeting PD-1 signaling^{39–41}. However, PD-1 (*PDCD1*) was expressed in a very small subset of cells, and the most informative exhaustion markers in our cohort were co-expression of *LAG3* and *TIM3*. These co-inhibitory molecules limit T cell activation and expansion⁴² and are potentially targetable using blocking antibodies⁴³. Therefore, these results suggest that the use of *LAG3* and/or *TIM3* blockade after infusion might improve efficacy in patients with poor EMR. The association between T cell exhaustion signatures in autologous infusion products and adverse patient characteristics also suggests that allogeneic CAR T cells, which are currently under clinical development, might be more beneficial in some patients. However, this requires further validation, as previous studies have not identified any association between patient characteristics and response⁴.

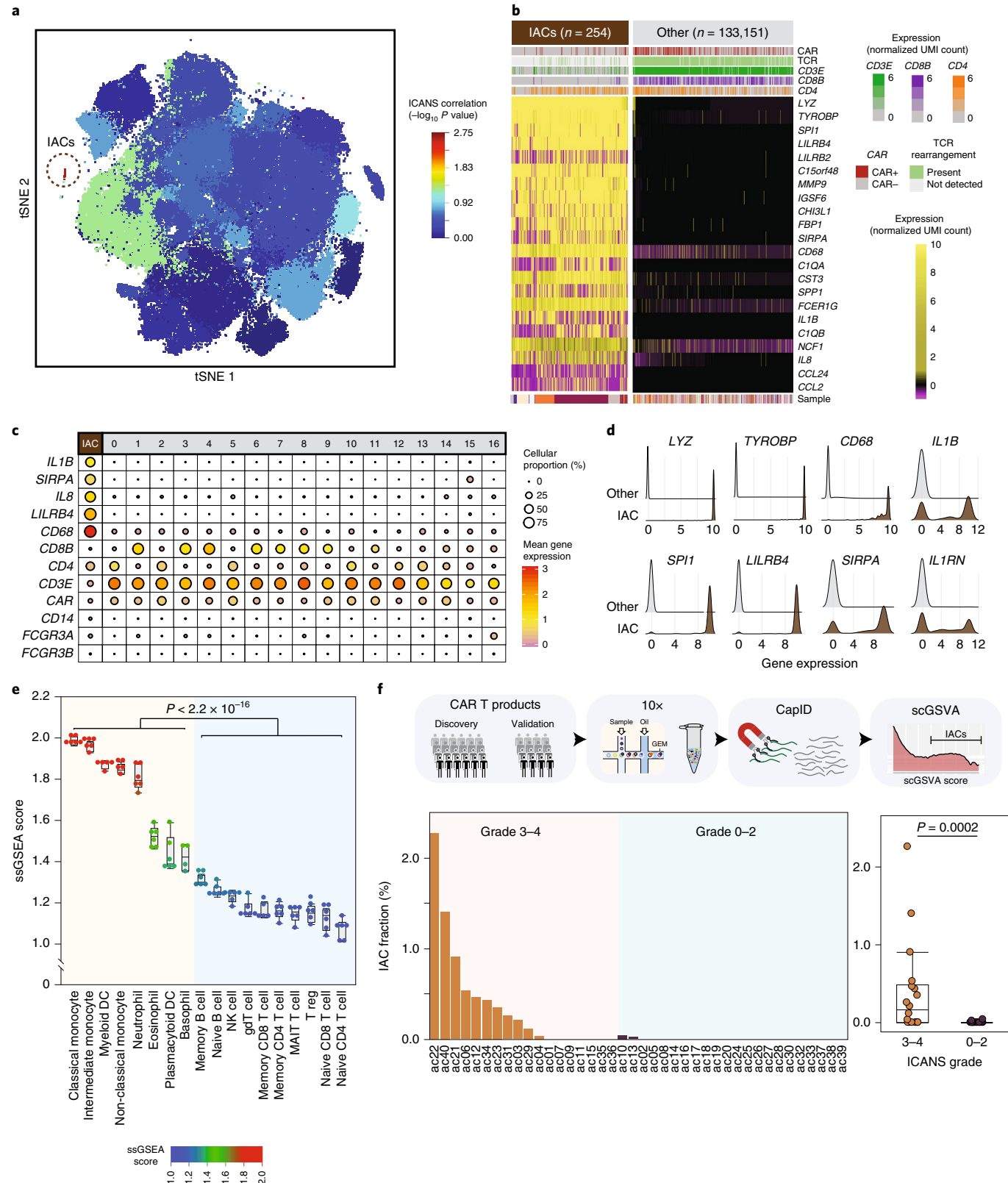
Finally, we identified a rare monocyte-like cell population within axi-cel infusion products that was significantly associated with the development of high-grade ICANS. The mechanism by which IACs might act in vivo to promote neurotoxicity is unclear, although IL-1 signaling has been recently implicated in the pathogenesis of ICANS²⁰, and the expression of *IL1B* and other inflammatory cytokines was significantly higher in IACs than in other cells within the infusion products. The association between this cell population and the development of high-grade ICANS requires validation and characterization by orthogonal approaches to scRNA-seq in a large prospective series, including

Fig. 6 | IACs in CD19 CAR T cell infusion products. **a**, Clusters are shown for 10x transcriptome data of 24 patients in a tSNE plot, colored by the significance of their association with ICANS. The significant cluster of IACs is circled. P values were calculated using a two-sided Wilcoxon rank-sum test. **b**, Genes that are most highly expressed in cells from the IAC cluster compared to cells from other clusters are shown in a heat map. Expression of additional T cell markers, TCR gene rearrangements and the CAR transcript are shown in tracks at the top. **c**, The expression of representative IAC markers, T cell markers and canonical monocyte markers are shown for each cluster. The size of bubbles is relative to the percentage of cells within a cluster that express a given gene, and the color is relative to the mean expression of a given gene within each cluster. **d**, Density plots show the cellular distribution of transcript abundance of IAC marker genes in cells from the IAC cluster compared to cells from other clusters, determined by 10x transcriptome data. **e**, ssGSEA values are shown for the IAC signature genes within gene expression data from purified populations of normal hematopoietic cell subsets, with increasing scores representing higher expression of the gene set. Myeloid lineage subsets (left, peach) have a significantly higher expression of genes that are characteristic of the IAC cluster compared to lymphoid lineage cells (two-sided Wilcoxon rank-sum test, $P < 2.2 \times 10^{-16}$). The highest expression of the IAC signature genes observed in monocytes. $n = 6$ for all cell types except for basophils ($n = 4$), myeloid DCs ($n = 5$), non-classical monocytes ($n = 5$) and memory CD8 T cells ($n = 5$). Boxes, median \pm the interquartile range; whiskers, 1.5x interquartile range. **f**, The cellular proportion of IACs determined by measurement of signature genes by CapID. The infusion products of 269,164 single cells from 40 patients' CAR T cell infusion products (24-patient discovery cohort and 16-patient validation cohort (bold sample ID)) are shown. The samples are grouped according to patients with grade 3–4 ICANS ($n = 18$, orange) compared to patients with grade 0–2 ICANS ($n = 22$, blue). Box, median \pm interquartile range; whiskers, 1.5x interquartile range. P values were calculated by a two-sided Wilcoxon rank-sum test.

the evaluation of whether they are present in products from other manufacturers.

Future studies should be conducted to validate the potential predictive capacity of day 7 molecular response and whether rational therapeutic interventions can be made in high-risk patients to

improve their outcomes. Furthermore, future studies should determine whether the detection of IACs within infusion products might identify a subset of patients who are at high risk of neurotoxicity and would benefit from prophylactic therapy with agents that target myeloid cell function, such as IL-1 receptor antagonists⁴⁴.



Online content

Any methods, additional references, Nature Research reporting summaries, source data, extended data, supplementary information, acknowledgements, peer review information; details of author contributions and competing interests; and statements of data and code availability are available at <https://doi.org/10.1038/s41591-020-1061-7>.

Received: 14 September 2019; Accepted: 13 August 2020;

Published online: 5 October 2020

References

- Locke, F. L. et al. Long-term safety and activity of axicabtagene ciloleucel in refractory large B-cell lymphoma (ZUMA-1): a single-arm, multicentre, phase 1–2 trial. *Lancet Oncol.* **20**, 31–42 (2019).
- Schuster, S. J. et al. Tisagenlecleucel in adult relapsed or refractory diffuse large B-cell lymphoma. *N. Engl. J. Med.* **380**, 45–56 (2019).
- Shah, N. N. & Fry, T. J. Mechanisms of resistance to CAR T cell therapy. *Nat. Rev. Clin. Oncol.* **16**, 372–385 (2019).
- Neelapu, S. S. et al. Axicabtagene ciloleucel CAR T-cell therapy in refractory large B-cell lymphoma. *N. Engl. J. Med.* **377**, 2531–2544 (2017).
- Mueller, K. T. et al. Clinical pharmacology of tisagenlecleucel in B-cell acute lymphoblastic leukemia. *Clin. Cancer Res.* **24**, 6175–6184 (2018).
- Green, M. R. & Neelapu, S. S. Not so FASt: tumor cells resisting death drive CAR T-cell dysfunction. *Cancer Discov.* **10**, 492–494 (2020).
- Das, R. K., Vernau, L., Grupp, S. A. & Barrett, D. M. Naive T-cell deficits at diagnosis and after chemotherapy impair cell therapy potential in pediatric cancers. *Cancer Discov.* **9**, 492–499 (2019).
- Finney, O. C. et al. CD19 CAR T cell product and disease attributes predict leukemia remission durability. *J. Clin. Invest.* **130**, 2123–2132 (2019).
- Sommermeyer, D. et al. Chimeric antigen receptor-modified T cells derived from defined CD8⁺ and CD4⁺ subsets confer superior antitumor reactivity in vivo. *Leukemia* **30**, 492–500 (2016).
- Fraietta, J. A. et al. Determinants of response and resistance to CD19 chimeric antigen receptor (CAR) T cell therapy of chronic lymphocytic leukemia. *Nat. Med.* **24**, 563–571 (2018).
- Rossi, J. et al. Preinfusion polyfunctional anti-CD19 chimeric antigen receptor T cells are associated with clinical outcomes in NHL. *Blood* **132**, 804–814 (2018).
- Lee, D. W. et al. ASTCT consensus grading for cytokine release syndrome and neurologic toxicity associated with immune effector cells. *Biol. Blood Marrow Transplant.* **25**, 625–638 (2019).
- Neelapu, S. S. et al. Chimeric antigen receptor T-cell therapy - assessment and management of toxicities. *Nat. Rev. Clin. Oncol.* **15**, 47–62 (2018).
- Teachey, D. T. et al. Identification of predictive biomarkers for cytokine release syndrome after chimeric antigen receptor T-cell therapy for acute lymphoblastic leukemia. *Cancer Discov.* **6**, 664–679 (2016).
- Hay, K. A. et al. Kinetics and biomarkers of severe cytokine release syndrome after CD19 chimeric antigen receptor-modified T-cell therapy. *Blood* **130**, 2295–2306 (2017).
- Le, R. Q. et al. FDA approval summary: tocilizumab for treatment of chimeric antigen receptor T cell-induced severe or life-threatening cytokine release syndrome. *Oncologist* **23**, 943–947 (2018).
- Santomaso, B. D. et al. Clinical and biological correlates of neurotoxicity associated with CAR T-cell therapy in patients with B-cell acute lymphoblastic leukemia. *Cancer Discov.* **8**, 958–971 (2018).
- Taraseviciute, A. et al. Chimeric antigen receptor T cell-mediated neurotoxicity in nonhuman primates. *Cancer Discov.* **8**, 750–763 (2018).
- Gust, J. et al. Endothelial activation and blood-brain barrier disruption in neurotoxicity after adoptive immunotherapy with CD19 CAR-T cells. *Cancer Discov.* **7**, 1404–1419 (2017).
- Norelli, M. et al. Monocyte-derived IL-1 and IL-6 are differentially required for cytokine-release syndrome and neurotoxicity due to CAR T cells. *Nat. Med.* **24**, 739–748 (2018).
- Sade-Feldman, M. et al. Defining T cell states associated with response to checkpoint immunotherapy in melanoma. *Cell* **175**, 998–1013 (2018).
- Blackburn, S. D. et al. Coregulation of CD8⁺ T cell exhaustion by multiple inhibitory receptors during chronic viral infection. *Nat. Immunol.* **10**, 29–37 (2009).
- Doering, T. A. et al. Network analysis reveals centrally connected genes and pathways involved in CD8⁺ T cell exhaustion versus memory. *Immunity* **37**, 1130–1144 (2012).
- Quigley, M. et al. Transcriptional analysis of HIV-specific CD8⁺ T cells shows that PD-1 inhibits T cell function by upregulating BATF. *Nat. Med.* **16**, 1147–1151 (2010).
- Miller, B. C. et al. Subsets of exhausted CD8⁺ T cells differentially mediate tumor control and respond to checkpoint blockade. *Nat. Immunol.* **20**, 326–336 (2019).
- Man, K. et al. Transcription factor IRF4 promotes CD8⁺ T cell exhaustion and limits the development of memory-like T cells during chronic infection. *Immunity* **47**, 1129–1141 (2017).
- Li, H. et al. Dysfunctional CD8 T cells form a proliferative, dynamically regulated compartment within human melanoma. *Cell* **176**, 775–789 (2019).
- Goldrath, A. W., Luckey, C. J., Park, R., Benoit, C. & Mathis, D. The molecular program induced in T cells undergoing homeostatic proliferation. *PNAS* **101**, 16885–16890 (2004).
- Josefsson, S. E. et al. TIGIT and PD-1 mark intratumoral T cells with reduced effector function in B-cell non-Hodgkin lymphoma. *Cancer Immunol. Res.* **7**, 355–362 (2019).
- Scherer, F. et al. Distinct biological subtypes and patterns of genome evolution in lymphoma revealed by circulating tumor DNA. *Sci. Transl. Med.* **8**, 364ra155 (2016).
- Lee, B., Sharron, M., Montaner, L. J., Weissman, D. & Doms, R. W. Quantification of CD4, CCR5, and CXCR4 levels on lymphocyte subsets, dendritic cells, and differentially conditioned monocyte-derived macrophages. *PNAS* **96**, 5215–5220 (1999).
- Kazazi, F., Mathijss, J. M., Foley, P. & Cunningham, A. L. Variations in CD4 expression by human monocytes and macrophages and their relationships to infection with the human immunodeficiency virus. *J. Gen. Virol.* **70**, 2661–2672 (1989).
- Uhlen, M. et al. A genome-wide transcriptomic analysis of protein-coding genes in human blood cells. *Science* **366**, eaax9198 (2019).
- Gargett, T., Truong, N., Ebert, L. M., Yu, W. & Brown, M. P. Optimization of manufacturing conditions for chimeric antigen receptor T cells to favor cells with a central memory phenotype. *Cytotherapy* **21**, 593–602 (2019).
- Wang, J. et al. Histone deacetylase inhibitors and IL21 cooperate to reprogram human effector CD8⁺ T cells to memory T cells. *Cancer Immunol. Res.* **8**, 794–805 (2020).
- Kurtz, D. M. et al. Noninvasive monitoring of diffuse large B-cell lymphoma by immunoglobulin high-throughput sequencing. *Blood* **125**, 3679–3687 (2015).
- Roschewski, M. et al. Circulating tumour DNA and CT monitoring in patients with untreated diffuse large B-cell lymphoma: a correlative biomarker study. *Lancet Oncol.* **16**, 541–549 (2015).
- Kurtz, D. M. et al. Circulating tumor DNA measurements as early outcome predictors in diffuse large B-cell lymphoma. *J. Clin. Oncol.* **36**, 2845–2853 (2018).
- Cherkassky, L. et al. Human CAR T cells with cell-intrinsic PD-1 checkpoint blockade resist tumor-mediated inhibition. *J. Clin. Invest.* **126**, 3130–3144 (2016).
- Gargett, T. et al. GD2-specific CAR T cells undergo potent activation and deletion following antigen encounter but can be protected from activation-induced cell death by PD-1 blockade. *Mol. Ther.* **24**, 1135–1149 (2016).
- Chong, E. A. et al. PD-1 blockade modulates chimeric antigen receptor (CAR)-modified T cells: refueling the CAR. *Blood* **129**, 1039–1041 (2017).
- Baumeister, S. H., Freeman, G. J., Dranoff, G. & Sharpe, A. H. Coinhibitory pathways in immunotherapy for cancer. *Annu. Rev. Immunol.* **34**, 539–573 (2016).
- Burugu, S., Dansok, A. R. & Nielsen, T. O. Emerging targets in cancer immunotherapy. *Semin. Cancer Biol.* **52**, 39–52 (2018).
- Strati, P. et al. Clinical efficacy of anakinra to mitigate CAR T-cell therapy-associated toxicity in large B-cell lymphoma. *Blood Adv.* **4**, 3123–3127 (2020).

Publisher's note Springer Nature remains neutral with regard to jurisdictional claims in published maps and institutional affiliations.

© The Author(s), under exclusive licence to Springer Nature America, Inc. 2020

Methods

Patient samples. Patients with DLBCL, tFL, PMBCL or high-grade B cell lymphoma being treated with axi-cel anti-CD19 CAR T cell as standard of care were eligible for this study. Those on active therapy at the time of their apheresis were excluded owing to potential confounding effects on the phenotype of CAR T cell infusion products. Patients provided informed consent for use of their cells and blood samples and the use and disclosure of de-identified health information in research as part of a protocol that was approved by the Institutional Review Board of The University of Texas MD Anderson Cancer Center. After completion of CAR T cell infusion, the infusion bag was washed with PBS to obtain residual cells. Samples were de-identified and transferred to the laboratory for scRNA-seq. At the 3-month follow-up, 13 patients had PD (50%), one was in PR (4%), nine were in CR (38%) and one was NE owing to death from sepsis. Peripheral blood samples from patients were drawn in ethylenediaminetetraacetic acid vacutainers at the time of a clinically indicated procedure and processed by centrifugation to obtain plasma. De-identified plasma from 24 healthy controls was obtained from the Gulf Coast Blood Center. Samples were available from patients at the infusion (days 0–1, $n=22$) and at 1 week (6–8 d, $n=22$), 2 weeks (12–18 d, $n=18$) and 1 month (25–35 d, $n=16$) after infusion. Analysis of cfDNA from patient samples and healthy controls was approved by the Institutional Review Board of The University of Texas MD Anderson Cancer Center.

Flow cytometry. When sufficient residual cells were available from CAR T cell infusion products, flow cytometry was performed using Horizon Fixable Viability Stain (BD Biosciences) and the following antibodies: CD134 FITC (ACT35, BD Biosciences), anti-CAR T PE (KIP-1, Kite Pharma), ICOS PE-TR (C398.4A, BD Biosciences), CD127 PerCP Cy5.5 (HIL-7R-M21, BD Biosciences), CD69 APC (FN50, BD Biosciences), CD28 APC-H7 (CD28.2, BD Biosciences), CD4 AF700 (RPA-T4, BD Biosciences), 4-1BB BV421 (4B4-1, BD Biosciences), CD14 BV605 (M5E2, BD Biosciences), CD8 BV650 (RPA-T8, BD Biosciences), CD3 BV711 (UCHT1, BD Biosciences) and PD-1 BV786 (EH12.1, BD Biosciences). All antibodies were used at the manufacturer's recommended concentration. Flow cytometry was performed on a BD Fortessa instrument, and the data were analyzed using Cytobank.

scRNA-seq. Fresh cells were interrogated using the 10 \times Chromium platform for simultaneous transcriptome and TCR profiling, with 133,405 cells (range, 1,732–8,573 cells per patient) passing our quality control (QC) thresholds and taken into subsequent analysis. These cells were sequenced to an average depth of 73,521 reads per cell, yielding an average of 2,472 genes per cell (Supplementary Fig. 1). All major TCR clonotypes had both CAR-positive and CAR-negative cells detected, suggesting no integration-site-driven jackpot effects⁴⁵ in this cohort.

5' gene expression profiling using 10 \times scRNA-seq was performed using the GemCodeTM single-cell platform and Chromium Single Cell 5' Reagent Kit (10 \times Genomics) according to the manufacturer's instructions. Briefly, CAR T cells were resuspended in PBS with 0.04% BSA and gently pipette mixed 10–15 times using a wide-bore pipette tip. Cell concentration was determined by cell counting with a hemocytometer, and an approximate concentration (between 700 and 1,200 cells per microliter) was adjusted to maximize the likelihood of achieving the desired cell recovery target. Samples were at least 85% viable cells confirmed by trypan blue stain before capture and always handled on ice when possible. Subsequently, single-cell suspension was mixed with RT Master Mix and loaded together with barcoded single-cell 5' gel beads and partitioning oil onto Single Cell A Chip to generate GEMs using Chromium Controller. Cell lysis and barcoded reverse transcription of RNAs from single cells were finished inside each GEM. Barcoded complementary DNA (cDNA) product was recovered through post GEM-RT cleanup and PCR amplification. cDNA QC and quantification were determined by High Sensitivity D5000 DNA ScreenTape analysis (Agilent Technologies) and Qubit dsDNA HS Assay Kit (Thermo Fisher Scientific). Fifty nanograms of cDNA was used for 5' Gene Expression library construction, and each sample was indexed by a Chromium i7 Sample Index Kit, which was run on an Illumina HiSeq4000 sequencer with 2 \times 100 base pairs (bp) paired reads to achieve a depth of at least 50,000 read pairs per cell.

Single-cell TCR repertoire sequencing. TCR α/β sequencing was performed with 10 \times Genomics Single Cell V(D)J Immune Profiling Solution (10 \times Genomics). Briefly, full-length V, D and J gene segments were amplified from barcoded cDNA using a Chromium Single Cell V(D)J Enrichment Kit (human T cells) to generate enrichment products. Enriched product was measured by D5000 DNA ScreenTape analysis and Qubit dsDNA HS Assay Kit, and then 50 ng of enrichment TCR product was used for library construction. Single Cell V(D)J enriched libraries were pooled for sequencing on HiSeq4000 to produce paired 2 \times 150 bp reads, taking into account depth requirement (5,000 read pairs per cell) between the pooled libraries.

Hybrid capture sequencing of marker genes of CapID. xGen Lockdown probes for 207 genes (Supplementary Table 2) were designed and synthesized by Integrated DNA Technologies (IDT). Hybridization capture of DNA libraries was performed

using xGen Hybridization and Wash Kit (IDT). First, pool 500 ng of each library to multiplex 8–12 libraries in a low-bind tube and add the blocker components, including Human Cot DNA and xGen blocking oligos. Dry down the mixture in a SpeedVac system. Second, thaw all contents of the xGen Hybridization and Wash Kit to room temperature and prepare the Hybridization Master Mix according to the manufacturer's protocol. Perform hybridization capture reaction in thermal cycler with 100 °C lid at the HYB program (95 °C, 30 s; 65 °C, overnight). Third, prepare wash buffers and equilibrate streptavidin beads at room temperature for a minimum of 30 min before performing the washes. In the thermal cycler with 70 °C lid, perform bead capture at 65 °C for 45 min. Every 10–12 min, gently pipette to ensure that the sample is fully resuspended. At the end of the 45 min, take the sample off the thermal cycler. Proceed immediately to heated washes and room temperature washes. Finally, perform post-capture PCR and purify post-capture PCR fragments. We employed 10% of post-capture elute as a template to run real-time quantitative PCR to determine the optimal number of PCR cycles for the custom probes panel. The captured library was measured using TapeStation System and Qubit dsDNA HS Assay Kit and run on Illumina MiSeq.

scRNA-seq bioinformatics. *Raw sequencing data processing, QC, data filtering and normalization.* The raw scRNA-seq data were pre-processed (demultiplex cellular barcodes, read alignment and generation of feature-barcode matrix) using Cell Ranger (10 \times Genomics, v2.1.1). Detailed QC metrics were generated and evaluated. Genes detected in fewer than three cells and cells where fewer than 200 genes had nonzero counts were filtered out and excluded from subsequent analysis. Low-quality cells where more than 15% of the read counts derived from the mitochondrial genome were also discarded. In addition, cells with more than 7,000 detected genes were discarded to remove likely doublet or multiplet captures. In this study, all sequencing libraries were constructed using the same version of reagent kits, by the same individual, following the same protocols, on the same 10 \times Chromium Controller, and the libraries were sequenced on the same Illumina HiSeq 4000 platform. The results of principal component analysis (PCA), t-distributed stochastic neighbor embedding (tSNE) plots and sample-by-cluster (Supplementary Fig. 1), flow-cell-by-cluster (Supplementary Fig. 10) and bead-lot-by-cluster (Supplementary Fig. 10) distribution were carefully reviewed, and integrated information revealed minimal batch effects. Seurat⁴⁶ was applied to the filtered gene-cell matrix to generate the normalized unique molecular identifier (UMI) counts as previously described⁴⁷.

Unsupervised cell clustering and dimensionality reduction. Seurat⁴⁶ v3.0.2 was applied to the normalized gene-cell matrix to identify highly variable genes. The elbow plot was generated with the *ElbowPlot* function of Seurat⁴⁶, and, based on which, the number of significant principal components (PCs) was determined. Different resolution parameters for unsupervised clustering were then examined to determine the optimal number of clusters. For this study, the first 20 PCs and 1,437 highly variable genes identified by Seurat⁴⁶ were used for unsupervised clustering analysis with the resolution set to 0.6, yielding a total of 17 cell clusters. The tSNE method was used for dimensionality reduction and two-dimensional visualization of the single-cell clusters.

Determination of major cell types and cell states. The major cell type (CD4 and CD8) was defined by marker gene expression (*CD4*, *CD40LG*, *TNFRSF4*, *CD8A* and *CD8B*) by 10 \times transcriptome and CapID sequencing data with an SNN boosting procedure. The functional state of each single cell (activated, memory, exhausted and regulatory) was determined using a hierarchical classification schema recently described by Sade-Feldman et al.²¹. All canonical marker genes in this schema were included on the CapID hybrid capture panel for sensitive detection (Supplementary Table 2), and cell type was automatically assigned to each individual cell based on the expression status of these genes²¹. On average, this supervised classification approach led to the unambiguous classification of 72.5% of T cells. CAR-positive T cells were identified by the presence (normalized UMI >0) of CAR-specific sequence contigs⁴⁸ (*FMC63-CD19scFV*, GenBank: HM852952.1) in the aligned reads, and this approach identified an average of 24% of QC-passed T cells as CAR positive (range, 7.1–42.6%). To describe the cell types and states that were defined by each tSNE cluster, we performed a manual review of the DEGs that were identified for each cell cluster by Seurat⁴⁶ (Extended Data Fig. 1 and Supplementary Table 12).

Capture-sequencing-based identification plus SNN boosting (CapID+) for cell type classification. Gene dropouts are common events in scRNA-seq data and represent a challenge for cell type identification. For the remaining unclassified cells (27.5%) in the above steps, we evaluated the gene dropout events and applied two strategies to improve cell type identification. First, we employed CapID sequencing data to assign positive and negative expression. Second, we applied an SNN boosting approach. Briefly, for each cell cluster, we first examined the diversity (the composition of cell types detected) and dominance ('purity', the proportion of cells in the cluster that are representative of a particular cell type) of classified cell types through a supervised approach, as described above. The cell type diversity of each cluster was evaluated by normalized Shannon entropy; the lower the Shannon entropy value, the lower the diversity and the higher the dominance of

a classified cell type within each individual cell cluster. SNN boosting was performed on the high-dominance clusters (dominance score ≥ 0.8 and normalized Shannon entropy ≤ 0.25 —the clusters that are dominated by a single cell type) with a cluster size of 50 or more cells. Cell type was assigned based on the hypothesis that phenotypically similar cells are grouped together, and cell type annotation was updated and used for SNN boosting in the next iteration. The boosting process was iterated on each cell cluster for 100 times (or when all unclassified cells were assessed). On average, this process rescued an additional 19.3% of cells in total (70% of unclassified cells) and improved the identification of CAR-positive cells from 24% to 35%.

Inferring cell cycle stage, hierarchical clustering, DEGs and pathway enrichment analysis. The cell cycle stage was computationally assigned to each individual cell using the R code implemented in Seurat⁴⁶ based on expression profiles of the cell-cycle-related signature genes, as previously described⁴⁹. DEGs were identified for each cluster using the *FindMarkers* function of the Seurat R package⁴⁶, and the DEG list was filtered with the following criteria: the gene should be expressed in 20% or more cells in the more abundant group; the absolute expression fold change should be greater than 1.2; and the false discovery rate (FDR) q value should be less than 0.05. Hierarchical clustering was performed for each cell type using Ward's minimum variance method. Heat maps were then generated using the *heatmap* function in pheatmap R package for filtered DEGs. For pathway analysis, the curated gene sets were downloaded from the Molecular Signature Database (<http://software.broadinstitute.org/gsea/msigdb/index.jsp>); ssGSEA was applied; and pathway scores were calculated for each cell using the GSVA software package⁵⁰. The CD8 T cell memory phenotype was defined by enrichment of a CD8 memory gene signature⁵¹ in CD8 subset, and the T cell dysfunction phenotype was defined by enrichment of T cell dysfunction-related markers⁵¹. Pathway enrichment analysis was done with the limma R software package. Significant signaling pathways were identified with FDR $q < 0.05$. Differences in *CD27*, *CCR7*, *LAG3* and *TIM3* (*HAVCR2*) that were identified by 10x whole-transcriptome data were validated by CapID to increase their sequencing saturation and, thereby, mitigate transcript dropout. There was no significant difference in the number of reads per cell between clinical response (CR versus PR/PD) or molecular response (>5FMR versus <5FMR) groups, further supporting little or no contribution of transcript dropout to differences observed between these groups (Supplementary Fig. 10).

Identification and characterization of the IAC cell cluster. To identify IAC cluster(s), we computed the proportion of cells assigned to a given cluster from each sample for the CRES-high and CRES-low/no groups and applied the two-sided Wilcoxon rank-sum test to determine the significance. P values were adjusted for multiple testing using the Benjamini–Hochberg method, and FDRs (q values) were calculated. The IAC cluster was then identified and characterized. IAC feature genes were identified by performed DEG analysis between the IAC and the rest of the other (non-IAC) cell clusters, and the top 20 highly variable DEGs were selected as the signature genes of IACs, followed by a manual evaluation and annotation process. To further determine the cell phenotype of IACs, we performed GSEA and calculated GSEA scores for the IAC signature genes using the curated gene expression data matrix from a genome-wide transcriptomic analysis of protein coding genes in human blood cells³³. The nonparametric two-sided Wilcoxon rank-sum test was used to determine the significance between the myeloid cell lineages (classical monocyte, intermediate monocyte, non-classical monocyte, myeloid dendritic cell (DC), neutrophil, basophil, eosinophil and plasmacytoid DC) and non-myeloid cell types (naive CD4 T cell, naive CD8 T cell, memory CD4 T cell, memory CD8 T cell, T regulatory cell, MAIT T cell, gdT cell, natural killer (NK) cell, naive B cell and memory B cell).

For each cell in the CapID data from the discovery ($n=24$) and validation ($n=16$) cohorts, the IAC gene signature score was calculated as the average gene expression level of IAC signature genes identified in the discovery cohort. IAC scores were first examined across cell clusters, which confirmed the expected significantly higher score in cells originally assigned to the IAC cluster ($P < 0.001$), as determined by their unique cell barcodes. IACs were, therefore, classified as cells with IAC signature gene scores greater than 1.5, which identified a total 440 IACs across 40 patients from the discovery and validation cohorts. The qualitative difference (present versus absent) between patients with grade 0–2 ICANS versus patients with grade 3–4 ICANS was tested using Fisher's exact test. The quantitative difference in IAC frequency between patients with grade 0–2 ICANS versus patients with grade 3–4 ICANS was tested using the Wilcoxon rank-sum test.

TCR V(D)J sequence assembly, paired clonotype calling, TCR diversity and clonality analysis and integration with scRNA-seq data. Cell Ranger v3.0.2 for V(D)J sequence assembly was applied for TCR reconstruction and paired TCR clonotype calling. The CDR3 motif was located, and the productivity was determined for each single cell. The clonotype landscape was then assessed, and the clonal fraction of each identified clonotype was calculated. The TCR clonotype diversity matrix was calculated using the tcr R package⁵². TCR clonality was defined as 1-Peilou's evenness and was calculated on productive rearrangements as previously described⁵³. Clonality values approaching 0 indicate a very even distribution of clone frequencies, whereas values approaching 1 indicate an increasingly

asymmetric distribution in which a few clones are present at high frequencies. The TCR clonotype data were then integrated with the T cell phenotype data inferred from single-cell gene expression analysis based on the shared cell barcodes.

Statistical analysis. In addition to the bioinformatics approaches described above for scRNA/TCR-seq data analysis, all other statistical analysis was performed using statistical software R v3.5.2. Analysis of differences in immunological features (continuous variables) between patient groups (R versus NR; CRES-high versus CRES-low/no) was determined by the nonparametric two-sided Wilcoxon rank-sum test. To control for multiple hypothesis testing, we applied the Benjamini–Hochberg method to correct P values, and the FDRs (q values) were calculated. All statistical significance testing was two sided, and results were considered statistically significant at $P < 0.05$. In R v3.5.2, 2.2×10^{-16} is the smallest value that can be accurately calculated⁵⁴. Therefore, some highly significant P values or q values are represented as $P < 2.2 \times 10^{-16}$ or $q < 2.2 \times 10^{-16}$, respectively.

cfDNA sequencing. **DNA extraction.** cfDNA was extracted from 2 ml of plasma for each time point using Qiagen Circulating Nucleic Acid Kit (Qiagen) and quality assessed using a TapeStation instrument and D1000 high-sensitivity tapes (Agilent Technologies). Genomic DNA was extracted from peripheral blood mononuclear cells of each patient using Qiagen AllPrep Mini Kit (Qiagen) and used as a germline control. DNA was quantified using Qubit high-sensitivity reagents (Thermo Fisher Scientific).

Library preparation, hybrid capture and sequencing. Libraries were prepared from up to 150 ng of cfDNA using Kapa Hyper Prep Kit (Roche) and XGen CS Adapters (IDT). In brief, DNA was end-repaired and a-tailed and then ligated using a 1:10 molar ratio of stubby duplex UMIs. Index-ligated products were cleaned up with AmPure beads (Beckman Coulter), subjected to up to eight cycles of PCR with oligos containing unique sequencing adapters and cleaned up with AmPure beads. Libraries were 12-plexed and captured using a 196-kb Nimblegen SeqCap EZ custom reagent (Roche) targeting previously described recurrently mutated regions⁵⁰. Enriched DNA was amplified with up to eight cycles of PCR, cleaned up with AmpPure beads and sequenced on a single lane of a HiSeq 4000 instrument using 100 bp paired-end reads at the MD Anderson Sequencing and Microarray Facility. Samples were sequenced to an average coverage of 12,427X (min, 5,921X; max, 21,856X).

Mutation detection and enumeration. The read data were demultiplexed into two read files and one UMI file, all in fastq format. The read files were first combined to form an unaligned BAM (uBAM) file with UMI information using the FastqToBam tool of fgbio version 0.6.1. An interleaved paired fastq file was generated using fgbio's SamToFastq tool and was used to align to the hg19 genome using BWA-MEM. UMI information was mapped from the uBAM file to the aligned reads using Picard 2.18.9/2.9.0's MergeBamAlignment tool. The alignments with UMI information then undergo several pre-processing steps using GATK version 3.7, including, in this order, indel realignment and two rounds of base quality recalibration. True PCR duplicates were then removed by using Picard's UmiAwareMarkDuplicatesWithMateCigar tool. Variants were called from the calibration time point (days 0–1) using the intersection of VarScan2 (ref. 54) and the GATK Unified Genotyper⁵⁵. Variants detected within sequencing of peripheral blood mononuclear cell samples from the same patient were treated as germline and filtered. Variants in repetitive elements, in the dbSNP data (build 151), in the ExAC database of 60,706 healthy individuals⁵⁶ or identified at VAFs of greater than 0.1% by deep sequencing of 24 healthy controls were filtered. An average of 11 variants were detected per patient (min 0, max 43; Supplementary Table 1), and 18 of 23 patients with available calibration samples passed the required threshold of three or more variants for subsequent monitoring. These variants were enumerated (supporting reads divided by total reads over the position) in data from each time point using Picard tools.

Definition of EMR. The fold change in VAF was calculated for each variant relative to the calibration time point. The mean of the fold changes for all variants was calculated for every patient at each time point. The day 6/7 fold change in VAF was tested for association with clinical response by dichotomizing patients into those who achieved CR versus those with PR or PD at their 3-month follow-up. The association between quantitative fold change in VAF and clinical response group was tested using a log-rank test. Patients were thereafter split into two groups of equal size with available follow-up data ($n=8$) using a five-fold reduction in VAF as the threshold, referred to as 5FMR.

Reporting Summary. Further information on research design is available in the Nature Research Reporting Summary linked to this article.

Data availability

All requests for raw and analyzed data and materials are promptly reviewed by The University of Texas MD Anderson Cancer Center to verify if the request is subject to any intellectual property or confidentiality obligations. Patient-related data not included in the paper might be subject to patient confidentiality. Any data and materials that can be shared will be released via a Material Transfer Agreement.

Transcriptome and CapID scRNA-seq data sets are available through the Gene Expression Omnibus (<https://www.ncbi.nlm.nih.gov/geo/>) under accessions GSE150992 and GSE151511, respectively. Raw data used in the generation of Figs. 1–6 and Extended Data Figs. 1–10 are available through the European Genome-phenome Archive (<https://www.ebi.ac.uk/ega/home>): accessions EGAD00001006327 and EGAD00001006325.

References

45. Fraietta, J. A. et al. Disruption of TET2 promotes the therapeutic efficacy of CD19-targeted T cells. *Nature* **558**, 307–312 (2018).
46. Butler, A., Hoffman, P., Smibert, P., Papalexi, E. & Satija, R. Integrating single-cell transcriptomic data across different conditions, technologies, and species. *Nat. Biotechnol.* **36**, 411–420 (2018).
47. Savas, P. et al. Single-cell profiling of breast cancer T cells reveals a tissue-resident memory subset associated with improved prognosis. *Nat. Med.* **24**, 986–993 (2018).
48. Kochenderfer, J. N. et al. Construction and preclinical evaluation of an anti-CD19 chimeric antigen receptor. *J. Immunother.* **32**, 689–702 (2009).
49. Jerby-Arnon, L. et al. A cancer cell program promotes T cell exclusion and resistance to checkpoint blockade. *Cell* **175**, 984–997 e924 (2018).
50. Hanzelmann, S., Castelo, R. & Guinney, J. GSVA: gene set variation analysis for microarray and RNA-seq data. *BMC Bioinf.* **14**, 7 (2013).
51. van der Leun, A. M., Thommen, D. S. & Schumacher, T. N. CD8⁺ T cell states in human cancer: insights from single-cell analysis. *Nat. Rev. Cancer* **20**, 218–232 (2020).
52. Nazarov, V. I. et al. tcR: an R package for T cell receptor repertoire advanced data analysis. *BMC Bioinf.* **16**, 175 (2015).
53. Reuben, A. et al. TCR repertoire intratumor heterogeneity in localized lung adenocarcinomas: an association with predicted neoantigen heterogeneity and postsurgical recurrence. *Cancer Discov.* **7**, 1088–1097 (2017).
54. Koboldt, D. C. et al. VarScan 2: somatic mutation and copy number alteration discovery in cancer by exome sequencing. *Genome Res.* **22**, 568–576 (2012).
55. McKenna, A. et al. The genome analysis toolkit: a MapReduce framework for analyzing next-generation DNA sequencing data. *Genome Res.* **20**, 1297–1303 (2010).
56. Lek, M. et al. Analysis of protein-coding genetic variation in 60,706 humans. *Nature* **536**, 285–291 (2016).

Acknowledgements

This work was supported by the Schweitzer Family Fund (J.R.W., R.E.D. and M.R.G.), The University of Texas MD Anderson Cancer Center B-Cell Lymphoma Moonshot (S.S.N. and M.R.G.), a National Cancer Institute Cancer Center Support Grant to The University of Texas MD Anderson Cancer Center (P30 CA016672) and Institutional Research Grant start-up research funds provided to L.W. and M.R.G. by The University of Texas MD Anderson Cancer Center. H.Y. is supported by a Fellow Award from the

Leukemia and Lymphoma Society. M.R.G. is supported by a Scholar Award from the Leukemia and Lymphoma Society.

Author contributions

Q.D., G.H., N.P.-O., M.C.J.M., N.J., H.Y., J.S., S.G., Q.Z. and S.P. performed experiments. L.W. and M.R.G. supervised the bioinformatics analysis. G.H., M.C., J.M., B.C., P.S., R.S., E.D., M.D., Y.W., S.Z., R.W., R.C., R.E.D., S.S.N., L.W. and M.R.G. analyzed data. F.H., L.F., F.S., H.C.L., L.J.N., N.F., J.W. and S.S.N. provided patient care. M.R.G. and S.S.N. conceived the study. M.R.G., L.W. and S.S.N. supervised the study and wrote the manuscript. All authors read and approved the manuscript.

Competing interests

B.C. reports advisory board membership for Advanced Accelerator Application and Clovis Oncology. N.F. reports advisory board membership for Roche, BMS, Gilead and Novartis; research funding from Roche, BMS, Novartis and BostonGene; and employment from BostonGene. H.C.L. reports consulting fees from Adaptive Biotechnologies, Amgen, Celgene, GlaxoSmithKline, Janssen, Sanofi and Takeda Pharmaceuticals and research funding from Amgen, Celgene, Daiichi Sankyo, GlaxoSmithKline, Janssen, Regeneron and Takeda Pharmaceuticals. L.J.N. reports personal fees and research fees from Celgene, Genentech, Juno, Merck and TG Therapeutics and personal fees from Bayer, Novartis and Spectrum Pharmaceuticals. J.W. reports advisory board membership for Kite/Gilead, Juno/Celgene/BMS, Novartis, Genentech, Janssen, Amgen, AstraZeneca, Curis and Morphosys and research funding from Kite/Gilead, June/Celgene/BMS, Novartis, Genentech, Janssen, AstraZeneca, 47, Unum Therapeutics, Curis and Morphosys. S.S.N. has received research support from Kite/Gilead, Collectis, Poseida, Merck, Acerta, Karus, BMS, Unum Therapeutics, Allogene and Precision Biosciences; has served as consultant and advisory board member for Kite/Gilead, Celgene, Novartis, Unum Therapeutics, Pfizer, Merck, Precision Biosciences, Cell Medica, Incyte, Allogene, Calibr and Legend Biotech; has received royalty income from Takeda Pharmaceuticals; and has patents related to cell therapy. M.R.G. reports consulting for VeraStem Oncology and stock ownership interest in KDac Therapeutics.

Additional information

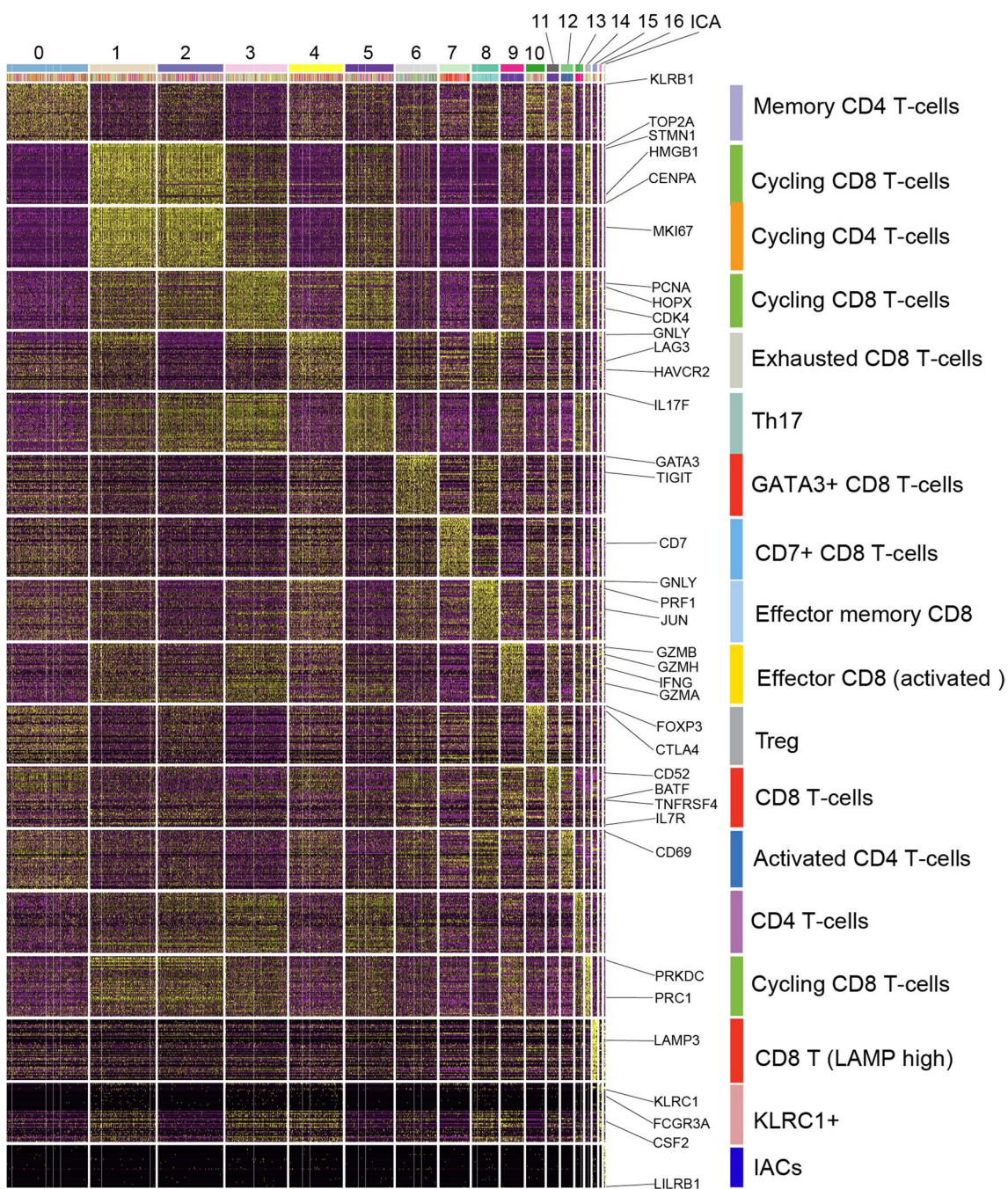
Extended data is available for this paper at <https://doi.org/10.1038/s41591-020-1061-7>.

Supplementary information is available for this paper at <https://doi.org/10.1038/s41591-020-1061-7>.

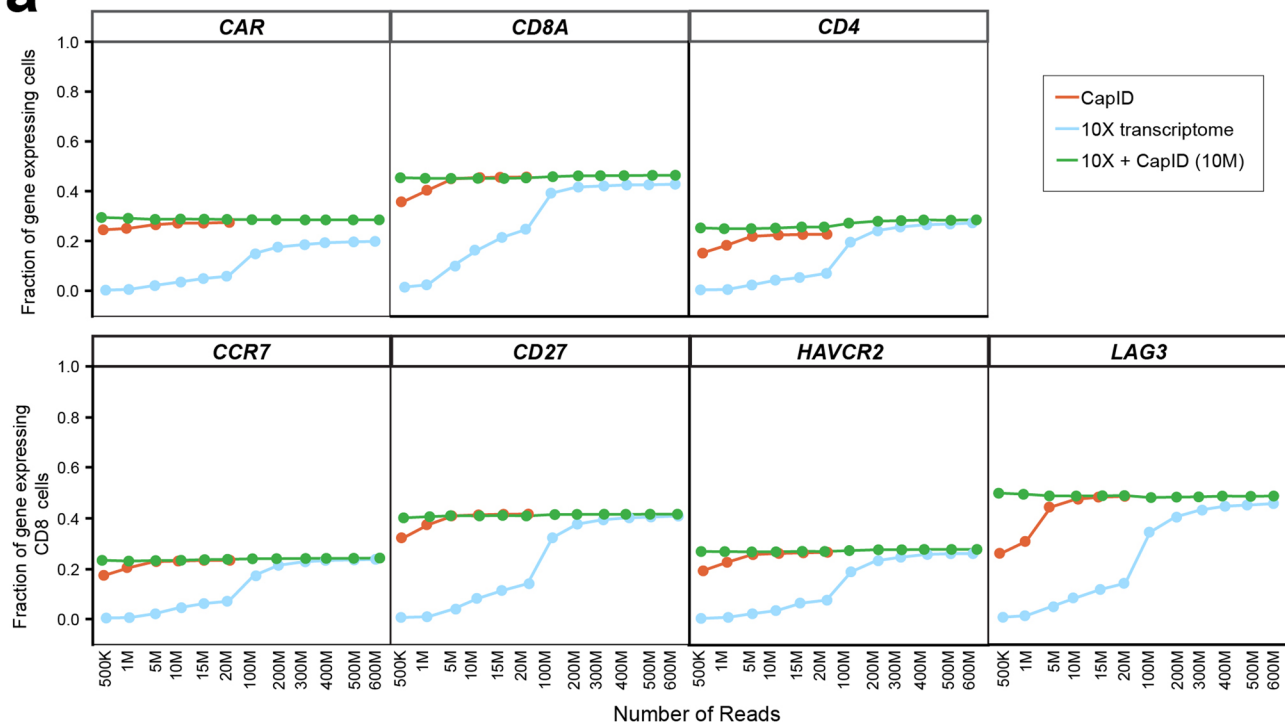
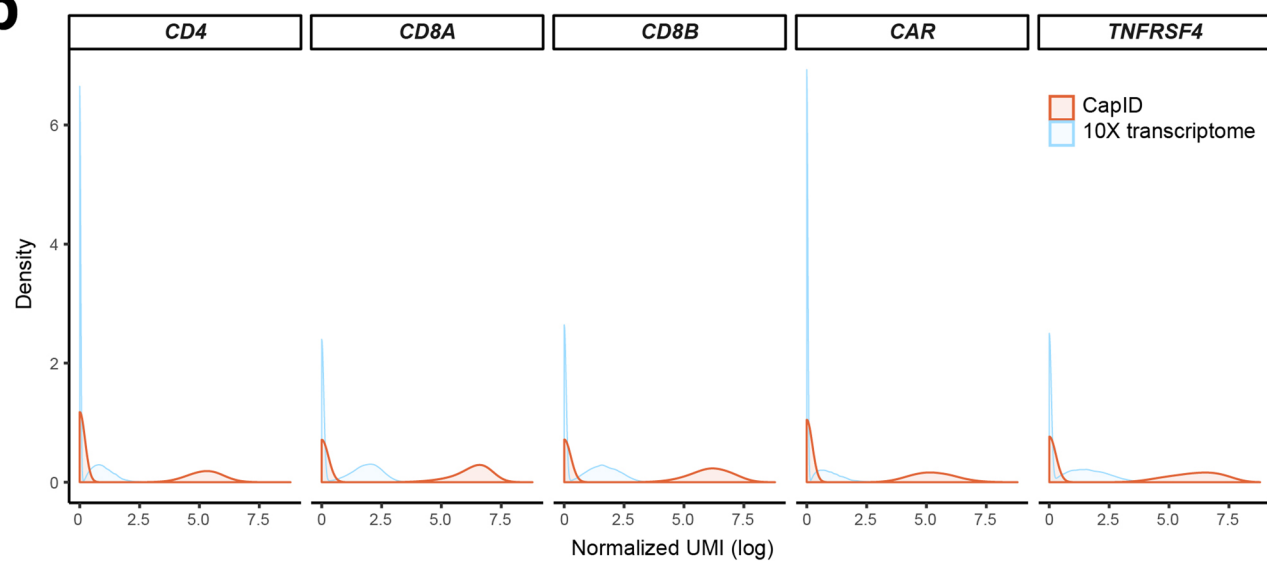
Correspondence and requests for materials should be addressed to S.S.N., L.W. or M.R.G.

Peer review information Saheli Sadanand was the primary editor on this article and managed its editorial process and peer review in collaboration with the rest of the editorial team.

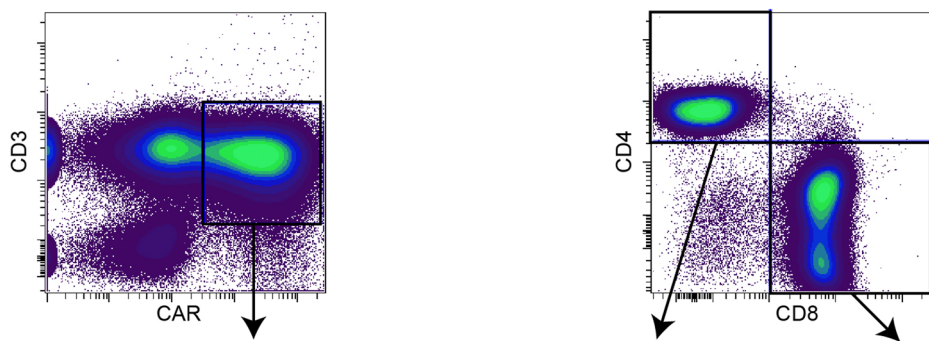
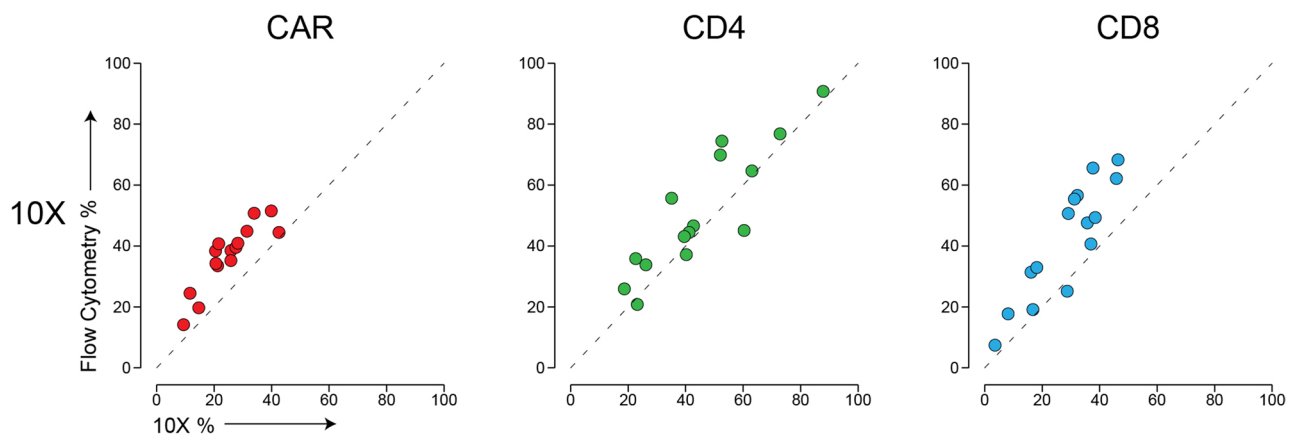
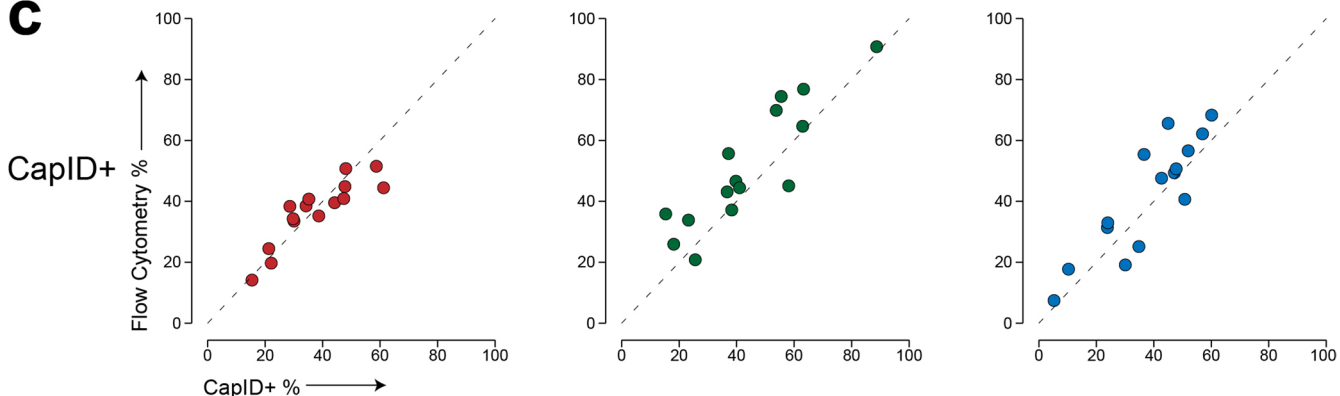
Reprints and permissions information is available at www.nature.com/reprints.



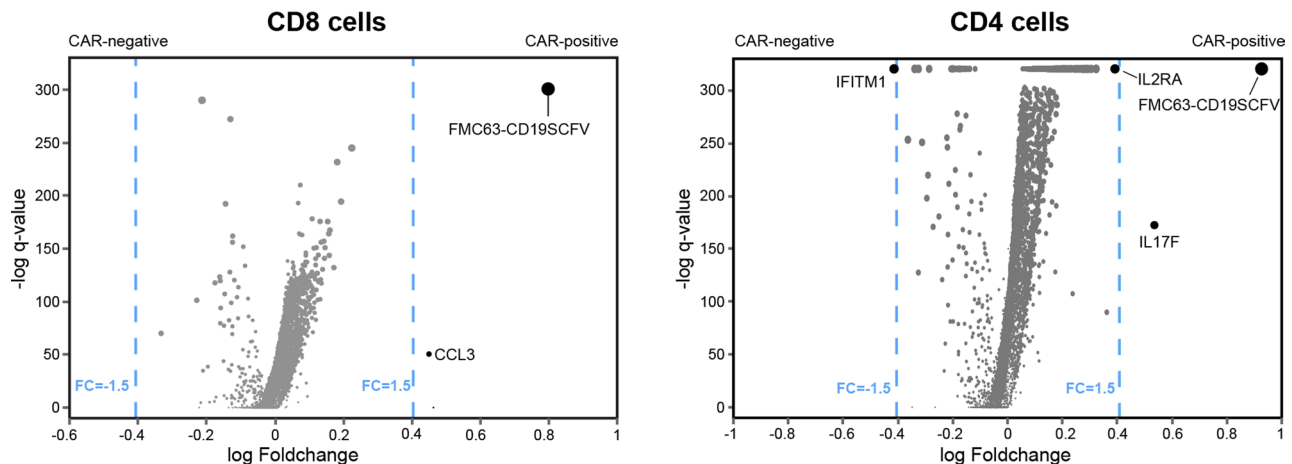
Extended Data Fig. 1 | Heatmap showing the top 50 signature genes of each cluster and putative assignments to cell types according to canonical marker genes.

a**b**

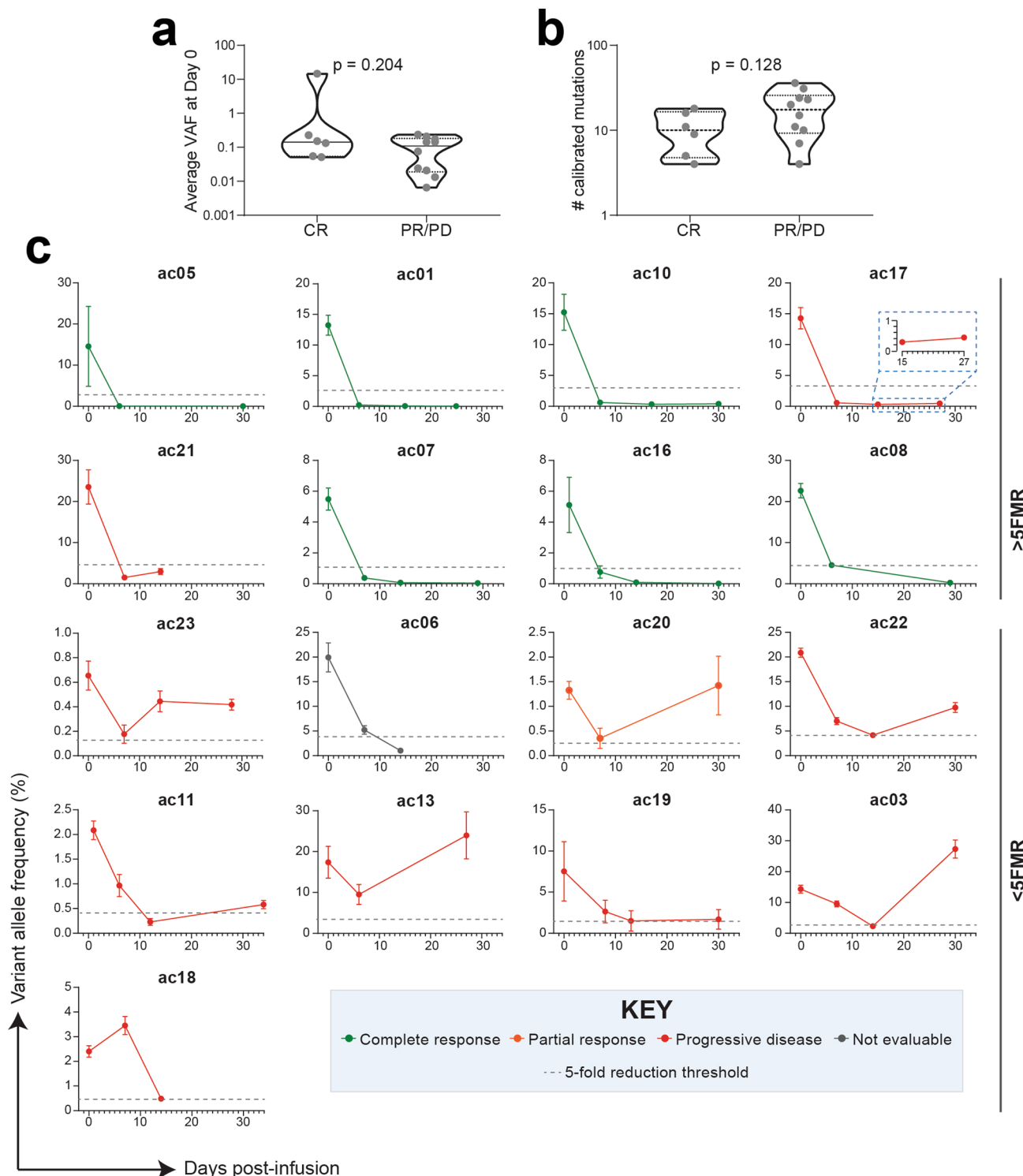
Extended Data Fig. 2 | Increased sequencing saturation and marker gene detection rate by CapID. **a**, Sub-sampling of reads from a single CAR T infusion product with 600 million reads for whole transcriptome and 20 million reads for CapID, showing the saturation (flattening of curve) for CapID (orange) at ~10 million reads, for 10X whole transcriptome sequencing (blue) at ~400 M reads, and the effect of supplementing whole transcriptome data with 10 million reads of CapID data (green). **b**, Density plots from the entire dataset show the reduced number of cells with UMI counts of zero and increased signal-to-noise ratio for CapID sequencing compared to 10X whole transcriptome sequencing. The 10X whole transcriptome sequencing in this study were performed to an average of 73,521 reads per cell, vastly exceeding the minimum of 20,000 reads per cell recommended by 10X.

a**b****c**

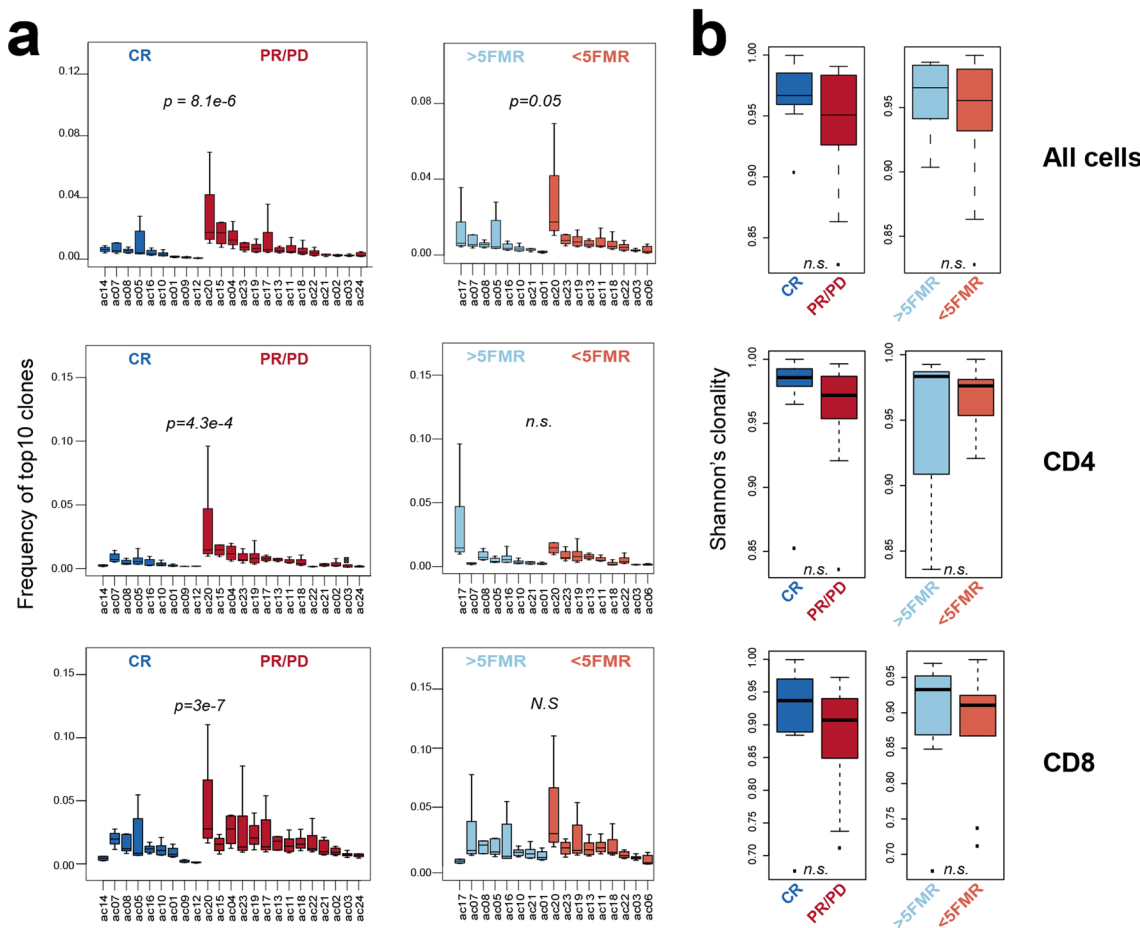
Extended Data Fig. 3 | Correlation of cell frequencies measured by scRNA-seq and flow cytometry. Correlations are shown for 16 patients that had sufficient cells for flow cytometry (a), compared to the fractions measured using traditional 10X data (b) or CapID+ (c). All comparisons showed a significant correlation with Pearson's correlation 2-tailed P-value < 0.001.



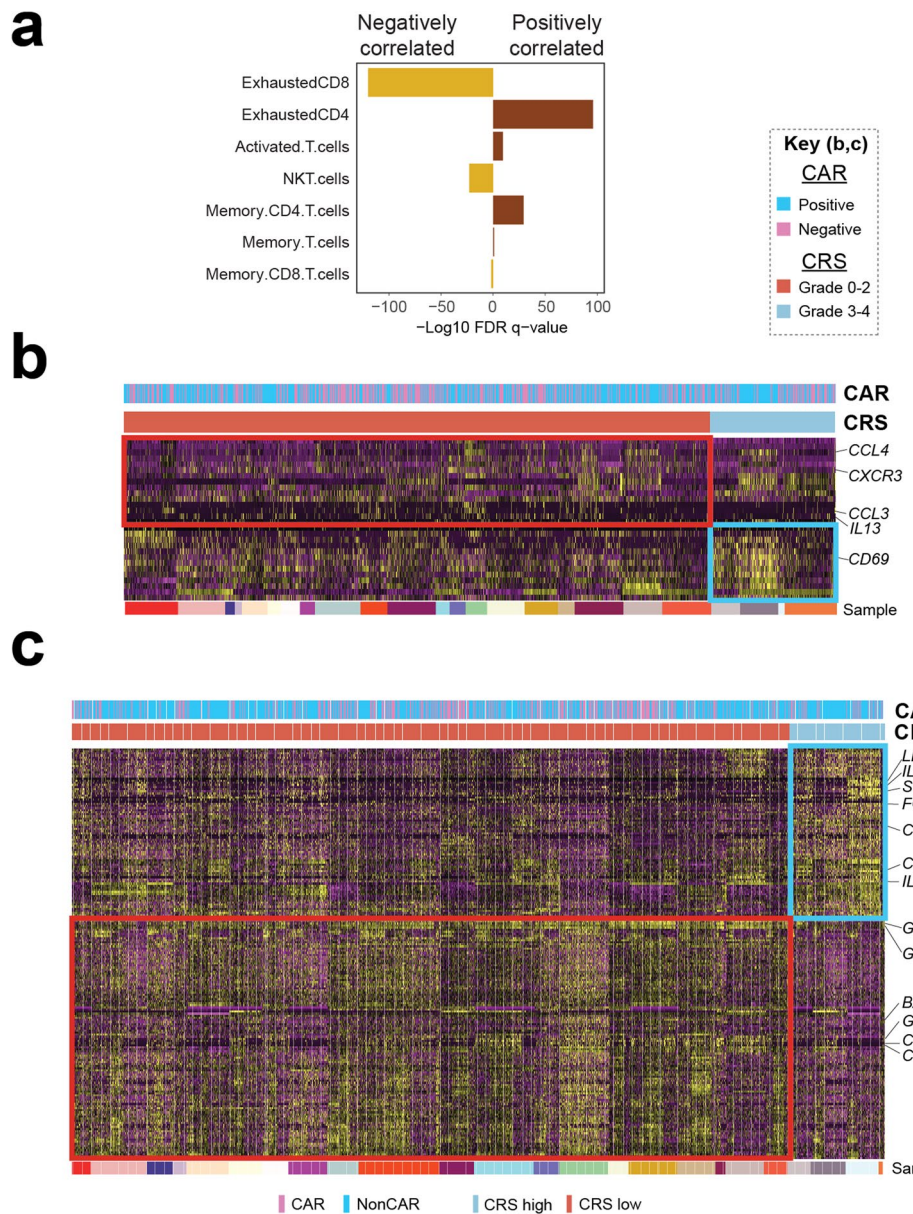
Extended Data Fig. 4 | Volcano plots of differentially expressed genes between CAR-positive and CAR-negative CD8 and CD4 T-cells. Q-values were calculated with a two-sided Wilcoxon rank sum test with Bonferroni correction.



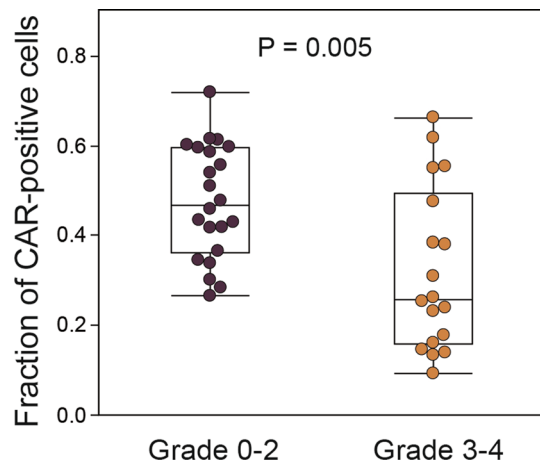
Extended Data Fig. 5 | Variant allele fractions of somatic variants detected by cfDNA sequencing. **a, b**, Comparison of the average VAF of mutations at day 0 (**a**) and the number of calibrated mutations (**b**) between clinical response groups. P values were calculated by a two-sided Student's t-test. **c**, Raw variant allele frequencies for each patient are shown for >5FMR (above) and <5FMR (below) groups. Lines are colored by clinical response as in Fig. 4a. The grey dashed line represents the 5-fold reduction threshold for each patient.



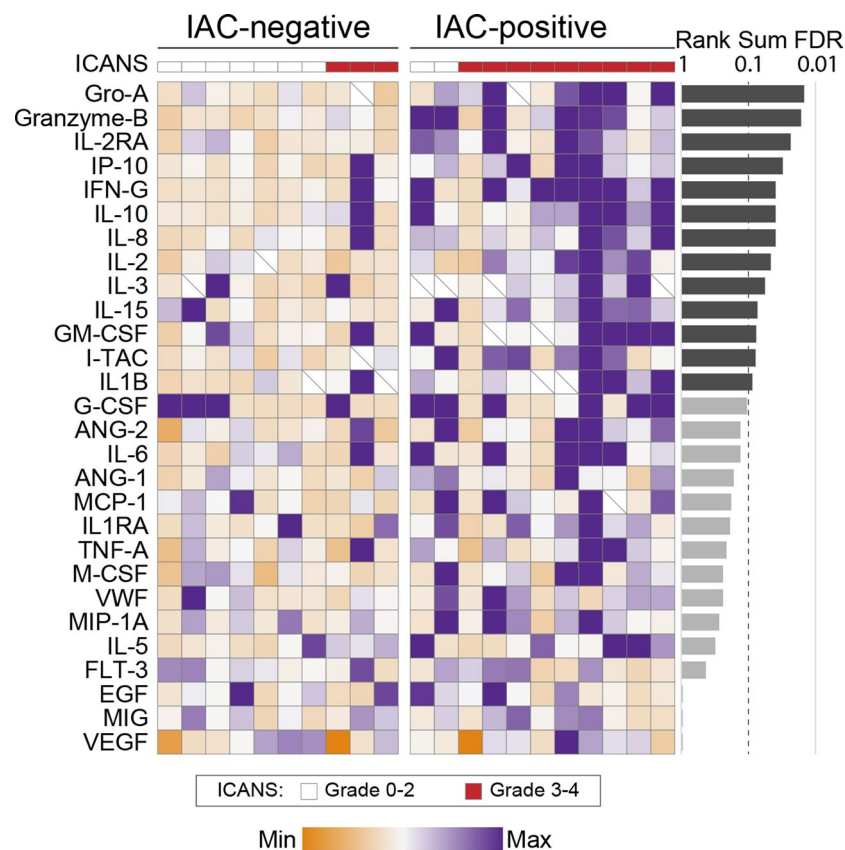
Extended Data Fig. 6 | T-cell clonotypic diversity in patients grouped by clinical and molecular response. **a**, The frequency of the top 10 clonotypes for each patient among all cells (above), CD4 T-cells (middle) and CD8 T-cells (below). Box, median \pm interquartile range. Whiskers, minimum and maximum. P-values calculated by a two-sided Wilcoxon rank sum test with Benjamini-Hochberg correction. **b**, Shannon's clonality score for patients grouped by clinical or molecular response, shown for all cells (above), CD4 T-cells (middle) and CD8 T-cells (below). CR, n = 9. PR/PD, n = 14. >5FMR, n = 8. <5FMR, n = 9. Box, median \pm interquartile range. Whiskers, minimum and maximum. P-values calculated by a two-sided Wilcoxon rank sum test with Benjamini-Hochberg correction.



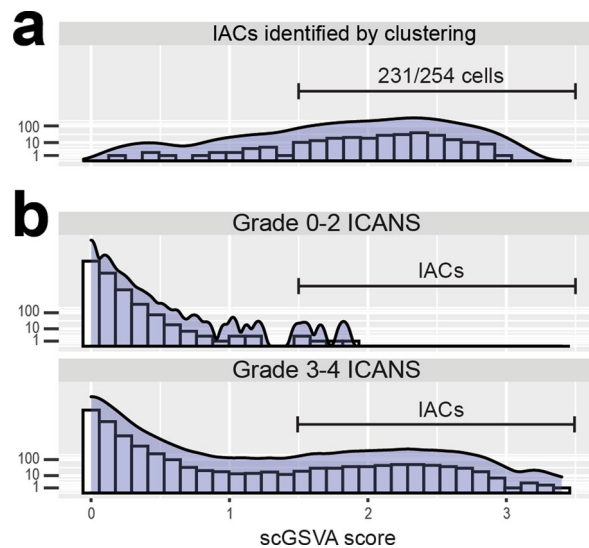
Extended Data Fig. 7 | Analysis of association between molecular features of CAR T-cell infusion products and the development of high-grade cytokine release syndrome (CRS). **a**, Comparison of functional states between patients with grade 0-2 and grade 3-4 identified reduced frequencies of exhausted CD8 T-cells and increased frequencies of exhausted CD4 T-cells to be associated with the development of high-grade CRS. Q-values were calculated by a two-sided Fisher exact test with a Benjamini-Hochberg correction. **b, c**, Heatmaps show differentially expressed genes between CD4 T-cells (**b**) and CD8 T-cells. (**c**) from the infusion products of patients with grade 0-2 CRS versus those that developed grade 3-4 CRS. The *CD69* gene shows higher expression and the *CCL3* and *CCL4* genes show lower expression on both CD4 and CD8 T-cells from the CAR T-cell infusion products of patients that developed high grade CRS. All differentially expressed genes are shown in Supplementary Tables 10, 11.



Extended Data Fig. 8 | Percentage of CAR-positive cells in patients with grade 0-2 vs grade 3-4 ICANS. Grade 0-2 ICANS, n=22. Grade 3-4 ICANS, n=18. Box, median \pm interquartile range. Whiskers, minimum and maximum. P-values calculated by a two-sided Wilcoxon rank-sum test.



Extended Data Fig. 9 | Cytokine levels in serum between patients with IACs and those without IACs. Significance level was tested with Mann-Whitney U test. FDR q-value was calculated for multiple testing correction.



Extended Data Fig. 10 | Quantification of the ICANS-associated cells (IACs) signature by scGSVA in CAR T-cell infusion products. **a**, A stringent threshold was set to ensure high confidence classification of IACs by scGSVA analysis of the 109 signature genes measured by CapID, as shown for the cells that were originally identified as IACs by unsupervised clustering of 10X whole-transcriptome data in Fig. 4a. **b**, The distribution of scGSVA scores shows a clear difference between infusion products from patients with grade 0-2 ICANS vs patients with grade 3-4 ICANS. The threshold for classification of cells as IACs (scGSVA score >1.5) is shown.

Reporting Summary

Nature Research wishes to improve the reproducibility of the work that we publish. This form provides structure for consistency and transparency in reporting. For further information on Nature Research policies, see [Authors & Referees](#) and the [Editorial Policy Checklist](#).

Statistics

For all statistical analyses, confirm that the following items are present in the figure legend, table legend, main text, or Methods section.

n/a Confirmed

- The exact sample size (n) for each experimental group/condition, given as a discrete number and unit of measurement
- A statement on whether measurements were taken from distinct samples or whether the same sample was measured repeatedly
- The statistical test(s) used AND whether they are one- or two-sided
Only common tests should be described solely by name; describe more complex techniques in the Methods section.
- A description of all covariates tested
- A description of any assumptions or corrections, such as tests of normality and adjustment for multiple comparisons
- A full description of the statistical parameters including central tendency (e.g. means) or other basic estimates (e.g. regression coefficient) AND variation (e.g. standard deviation) or associated estimates of uncertainty (e.g. confidence intervals)
- For null hypothesis testing, the test statistic (e.g. F , t , r) with confidence intervals, effect sizes, degrees of freedom and P value noted
Give P values as exact values whenever suitable.
- For Bayesian analysis, information on the choice of priors and Markov chain Monte Carlo settings
- For hierarchical and complex designs, identification of the appropriate level for tests and full reporting of outcomes
- Estimates of effect sizes (e.g. Cohen's d , Pearson's r), indicating how they were calculated

Our web collection on [statistics for biologists](#) contains articles on many of the points above.

Software and code

Policy information about [availability of computer code](#)

Data collection

No external data were used in this study. All single cell RNA sequencing data were generated locally in our laboratory at MD Anderson Cancer Center. Software used on Illumina HiSeq 4000 and for demuxing included HiSeq Control Software (HSC) version HD 3.4.0.38, Real time Analysis (RTA) version 2.7.7, and bcl2fastq version 2.20.0.

Data analysis

Data analysis was performed using CellRanger v2.1.1, R v3.5.2, Seurat v3.0.2 (R package), limma (R package), pheatmap (R package), SPSS v24, GraphPad Prism v8, and Cytobank.

For manuscripts utilizing custom algorithms or software that are central to the research but not yet described in published literature, software must be made available to editors/reviewers. We strongly encourage code deposition in a community repository (e.g. GitHub). See the Nature Research [guidelines for submitting code & software](#) for further information.

Data

Policy information about [availability of data](#)

All manuscripts must include a [data availability statement](#). This statement should provide the following information, where applicable:

- Accession codes, unique identifiers, or web links for publicly available datasets
- A list of figures that have associated raw data
- A description of any restrictions on data availability

All sequencing data will be deposited in the European Genome-Phenome Archive upon acceptance of the manuscript.

Field-specific reporting

Please select the one below that is the best fit for your research. If you are not sure, read the appropriate sections before making your selection.

- Life sciences Behavioural & social sciences Ecological, evolutionary & environmental sciences

For a reference copy of the document with all sections, see nature.com/documents/nr-reporting-summary-flat.pdf

Life sciences study design

All studies must disclose on these points even when the disclosure is negative.

Sample size	scRNA sequencing and CapID from n = 24 samples from n= 24 patients for discovery analysis. Assuming a CR rate of 33%, a sample size of 24 would produce 8 subjects with CR and 16 subjects without. At these group sizes, a two-sided t-test controlling the Type I error rate at $\alpha=0.05$ would have more than 80% power to detect a difference in mean cell fractions equal to 1.4 times the common standard error. CapID was performed for IACs enumeration in a validation cohort of n=16 samples from n=16 patients.
Data exclusions	Patients that were on therapy at the time of apheresis were excluded from the study due to the potential confounding effect that this treatment could have of T-cell gene expression profiles. This criteria was pre-established.
Replication	Gene expression characteristics identified by transcriptome sequencing were validated by CapID. Association between IACs cell fraction identified in the 24 patient discovery cohort was validated in an independent 16 patient validation cohort. All attempts at replication were successful.
Randomization	NA
Blinding	ICANs grade of the 16 patient validation cohort was blinded until after the IACs percentage for these samples was calculated. Blinding was not performed in other parts of the study because this is a discovery analysis.

Reporting for specific materials, systems and methods

We require information from authors about some types of materials, experimental systems and methods used in many studies. Here, indicate whether each material, system or method listed is relevant to your study. If you are not sure if a list item applies to your research, read the appropriate section before selecting a response.

Materials & experimental systems		Methods	
n/a	Involved in the study	n/a	Involved in the study
<input type="checkbox"/>	<input checked="" type="checkbox"/> Antibodies	<input type="checkbox"/>	<input checked="" type="checkbox"/> ChIP-seq
<input checked="" type="checkbox"/>	<input type="checkbox"/> Eukaryotic cell lines	<input checked="" type="checkbox"/>	<input type="checkbox"/> Flow cytometry
<input checked="" type="checkbox"/>	<input type="checkbox"/> Palaeontology	<input checked="" type="checkbox"/>	<input type="checkbox"/> MRI-based neuroimaging
<input checked="" type="checkbox"/>	<input type="checkbox"/> Animals and other organisms		
<input type="checkbox"/>	<input checked="" type="checkbox"/> Human research participants		
<input checked="" type="checkbox"/>	<input type="checkbox"/> Clinical data		

Antibodies

Antibodies used	CD134 FITC (ACT35, BD Biosciences), anti-CAR T PE (KIP-1, Kite), ICOS PE-TR (C398.4A, BD Biosciences), CD127 PerCP Cy5.5 (HIL-7R-M21, BD Biosciences), CD69 APC (FN50, BD Biosciences), CD28 APC-H7 (CD28.2, BD Biosciences), CD4 AF700 (RPA-T4, BD Biosciences), 4-1BB BV421 (4B4-1, BD Biosciences), CD14 BV605 (M5E2, BD Biosciences), CD8 BV650 (RPA-T8, BD Biosciences), CD3 BV711 (UCHT1, BD Biosciences), PD-1 BV786 (EH12.1, BD Biosciences).
-----------------	---

Validation	CD134, CD69: Validated by manufacturer on human PHA-stimulated peripheral blood mononuclear cells anti-CAR (KIP1): validated by the manufacturer on CAR T-cells. ICOS, CD127, CD28, PD1, CD3, CD4, CD8, CD14: validated by the manufacturer on human peripheral blood mononuclear cells 4-1BB: validated on human Con A stimulated peripheral blood mononuclear cells
------------	--

Human research participants

Policy information about [studies involving human research participants](#)

Population characteristics	40 patients with a diagnosis of relapsed/refractory large B cell lymphoma receiving axi-cel CD19 CAR T-cells as standard of care. These included 26 males and 14 females with an average age of 57 (range 24-76). Plasma from 24 healthy controls was used for cfDNA sequencing analysis. These samples were fully deidentified and not accompanied by any demographical information.
----------------------------	---

Recruitment

All patients signed an informed consent for use of residual cells and clinical data for research purposes after meeting with a research nurse or study coordinator. The patients represented sets of 24 consecutive consenting patients for the discovery cohort and 16 consecutive consenting patients for the validation cohort. There was no selection for patient consenting or accrual.

Ethics oversight

These studies were approved by the Internal Review Board of MD Anderson Cancer Center. Approvals include the use of both patient samples and healthy control samples.

Note that full information on the approval of the study protocol must also be provided in the manuscript.